Sublattice scars and beyond in two-dimensional $U(1)$ quantum link lattice gauge theories

Indrajit Sau,[1] Paolo Stornati,[2] Debasish Banerjee,[3,4] and Arnab Sen[1]

[1]*School of Physical Sciences, Indian Association for the Cultivation of Science, Jadavpur, Kolkata 700032, India*

[2]*ICFO-Institut de Ciencies Fotoniques, The Barcelona Institute of Science and Technology, Mediterranean Technology Park, Avinguda Carl Friedrich Gauss, 3, 08860 Castelldefels, Barcelona, Spain*

[3]*Theory Division, Saha Institute of Nuclear Physics, 1/AF Bidhannagar, Kolkata 700064, India*

[4]*Homi Bhabha National Institute, Training School Complex, Anushaktinagar, Mumbai 400094, India*

(Received 23 November 2023; accepted 25 January 2024; published 27 February 2024)

In this article, we elucidate the structure and properties of a class of anomalous high-energy states of matter-free $U(1)$ quantum link gauge theory Hamiltonians using numerical and analytical methods. Such anomalous states, known as quantum many-body scars in the literature, have generated a lot of interest due to their athermal nature. Our starting Hamiltonian is $H = \mathcal{O}_{\text{kin}} + \lambda\mathcal{O}_{\text{pot}}$, where λ is a real-valued coupling, and $\mathcal{O}_{\text{kin}}$ ($\mathcal{O}_{\text{pot}}$) are summed local off-diagonal (diagonal) operators in the electric flux basis acting on the elementary plaquette $\square$. The spectrum of the model in its spin-$\frac{1}{2}$ representation on $L_x \times L_y$ lattices reveal the existence of sublattice scars, $|\psi_s\rangle$, which satisfy $\mathcal{O}_{\text{pot},\square}|\psi_s\rangle = |\psi_s\rangle$ for all elementary plaquettes on one sublattice and $\mathcal{O}_{\text{pot},\square}|\psi_s\rangle = 0$ on the other, while being simultaneous zero modes or nonzero integer-valued eigenstates of $\mathcal{O}_{\text{kin}}$. We demonstrate a "triangle relation" connecting the sublattice scars with nonzero integer eigenvalues of $\mathcal{O}_{\text{kin}}$ to particular sublattice scars with $\mathcal{O}_{\text{kin}} = 0$ eigenvalues. A fraction of the sublattice scars have a simple description in terms of emergent short singlets, on which we place analytic bounds. We further construct a long-ranged parent Hamiltonian for which all sublattice scars in the null space of $\mathcal{O}_{\text{kin}}$ become unique ground states and elucidate some of the properties of its spectrum. In particular, zero energy states of this parent Hamiltonian turn out to be exact scars of another $U(1)$ quantum link model with a staggered short-ranged diagonal term.

DOI: 10.1103/PhysRevD.109.034519

I. INTRODUCTION

Traditional high-energy physics has focused on the consideration of physical phenomena that typically happen at energy scales much greater than the ground state or even the relevant low-energy physics. This approach has been particularly useful in decoding the fundamental particles and their interactions in nature through a series of collider experiments at successively higher energies, culminating in the discovery of the Higgs particle [1]. The nature of the collider experiments is such that it is able to create matter at high energy densities, while having less control on the microscopic details of particular (eigen)states of interesting theories. This makes it extremely difficult to study the physics of isolated excited quantum states which may have interesting properties by themselves. Probing fragile quantum mechanical effects directly from collider experiments, such as entanglement, can be challenging, although there is recent work on studies of entanglement of particle pairs produced at the Large Hadron Collider [2,3].

In the past decade, the landscape of experiments available have highly expanded due to the remarkable success of tabletop experiments in controlling microscopic degrees of freedom in a very precise manner [4]. This has led to the construction of quantum simulators and quantum computers using a host of different architectures such as Rydberg atoms, superconducting qubits, and even photons trapped in a cavity (circuit QED) [5]. These experiments have enabled the use of measures of quantum entanglement, and more generally quantum information theory, in order to classify and understand a variety of physical phenomena which defy conventional wisdom. Therefore, dynamical aspects of various theories, notably those relating to thermalization, can be studied with these tabletop experiments considerably easily than in collider experiments. There has been proposals to mimic particle collisions in tabletop experiments to study their dynamics [6,7], as well as various other aspects of the physics which are

difficult to study using classical simulation methods [8–14]. Together with the original proposals, they have motivated the realization of lattice gauge theories in quantum computer and simulator setups [15–18].

Questions about the thermalization of many body quantum systems is also a central topic of investigation in condensed matter physics. The studies of thermalization in quantum spin and fermionic models have been guided by the so-called eigenstate thermalization hypothesis (ETH) [19–21]. ETH postulates that even though quantum mechanics allows for unitary dynamics of closed systems, a subsystem of the full system appears to thermalize, since the rest of the system acts as a heat bath for the subsystem under consideration, thereby establishing the validity of quantum statistical mechanics. A key result that has emerged from studies of ETH in the most common spin and fermionic model is that a state whose energy density is $O(J)$, $J \sim 1$ higher than the ground state thermalizes in time $t \sim O(1)$.

Simultaneously, there has also been an explosion of interest towards the investigation of scenarios in translationally invariant systems which show deviation from the conventional wisdom of ETH, both theoretically and experimentally [22–28]. Two such scenarios, weak ergodicity breaking and strong ergodicity breaking, have been theoretically proposed for translational invariant systems. The former scenario shows the presence of anomalous high-energy states, also dubbed as quantum many-body scars [22,23,29–50] in the spectrum of the Hamiltonian which often admit description in terms of an exponentially smaller number of Fock states (compared to neighboring nonanomalous high-energy states) with a simple physical interpretation. The latter scenario on the other hand, emerges when the symmetry resolved Hamiltonian further splits into exponentially many disconnected sectors without a clear description in terms of symmetries and no single dominant sector in the thermodynamic limit [25,26,51,52]. The reader is referred to Ref. [53] for a detailed review of the topics.

Lattice gauge theories, which possess a local invariance, and thus often used as microscopic models to explain a variety of phenomena in both high-energy and condensed matter physics, such as confinement [54–56], spin liquids [57], and superconductivity [58] have also been recently subjected to similar investigations for ETH violation scenarios without disorder. Quantum many-body scars have been established to be a reason for the anomalous thermalization observed in a pedagogical model [27,59]: the Schwinger model with quantum link gauge fields [60], also known as the PXP model [22,61,62] in condensed matter physics. Scars have been investigated in various kinds of Schwinger models and higher-spin PXP models [48,63,64]. Such anomalous states have also been uncovered in $\mathbb{Z}_2$ as well as certain non-Abelian gauge theories [65,66]. It has been shown that even two-dimensional matter free $U(1)$ gauge theories possess a rich variety of scars [67–69]. In fact, the particular two-dimensional microscopic models are those which are used in the context of spin-ice (the quantum link model) [70–72] and effective theories of quantum antiferromagnets (the quantum dimer model) [58,73–76], and are known as Rokhsar-Kivelson models. In the latter case, the presence of exponentially many (in the longer linear dimension) quantum many-body scars could be shown for ladder systems, called lego scars [69]. The structure of the quantum scars in the quantum link model has been comparatively elusive to identify.

In this article, we provide a systematic study of the quantum many-body scars of $U(1)$ quantum link models in their spin-$\frac{1}{2}$ representation and elucidate the structure of a class of scars. We call one variety of such scars as sublattice scars. These scars have the peculiar property of being localized in one of the two possible sublattices of a $L_x \times L_y$ lattice with both L_x, L_y being even due to interference effects associated with the flipping of elementary plaquettes caused by the off-diagonal operator $\mathcal{O}_{\text{kin}}$. While $\mathcal{O}_{\text{kin}}$ has an exponentially large number (in $L_x L_y$) of exact zero modes due to a particular index theorem [22,23,77], a typical zero mode is expected to mimic an infinite temperature thermal state locally and hence be completely featureless, as far as local features are concerned, from ETH. On the other hand, these sublattice scars display perfect ordering of the diagonal operator $\mathcal{O}_{\text{pot}}$, which counts the total number of plaquettes which can be flipped. More specifically, the local operator $\mathcal{O}_{\text{pot},\square}$ acting on each plaquette either takes its maximum value (1) or minimum (0) on the relevant sublattice. While most sublattice scars belong to the null space of $\mathcal{O}_{\text{kin}}$, there also exist sublattice scars with nonzero integer eigenvalues of $\mathcal{O}_{\text{kin}}$. We also unearth other anomalous zero modes of $\mathcal{O}_{\text{kin}}$, or quantum many-body scars, that are distinct from the sublattice scars. These scars turn out to be simultaneous zero modes of $\mathcal{O}_{\text{kin}}$ and another noncommuting diagonal term composed by summing $\mathcal{O}_{\text{pot},\square}$ over all elementary plaquettes of the lattice in a staggered fashion, depending on which sublattice the plaquette belongs to.

The rest of the article is organized as follows: Sec. II gives an account of two microscopic lattice gauge theory models with short-ranged Hamiltonians that we consider in our study, together with their local and global symmetries. Section III focuses on the description of sublattice scars that can either be anomalous zero modes of $\mathcal{O}_{\text{kin}}$ or are eigenstates of $\mathcal{O}_{\text{kin}}$ with eigenvalues ± 2. We discuss a class of sublattice scars which can be analytically constructed using short singlets on a dual square lattice, as well as those which cannot be formed using such a description. In Sec. IV, we describe an efficient numerical method to specifically generate sublattice scars that goes beyond brute force exact diagonalization (ED). In Sec. V, we formulate a long-range parent Hamiltonian whose ground state consists of all the sublattice scars of the original short-range

quantum link model with $\mathcal{O}_{\rm kin} = 0$. The sublattice scars with eigenvalues $\mathcal{O}_{\rm kin} = \pm 2$ can be given a quasiparticle-like description starting from particular ground states of this parent Hamiltonian. Some interesting properties of the spectrum of this parent Hamiltonian are also discussed. In particular, zero energy states of this parent Hamiltonian turn out to be exact anomalous midspectrum zero modes of another short-ranged quantum $U(1)$ link model, but with a staggered short-ranged diagonal term which is discussed in Sec. VI. We finally conclude and present some open directions in Sec. VII.

II. THE MODELS

The investigation of ETH or violations thereof in the context of lattice gauge theories is complicated by the fact that the traditional formulations of lattice gauge theories due to Wilson [78,79] use an infinite dimensional Hilbert space for each local degree of freedom. This allows for the presence of arbitrarily high energy eigenstates in the spectrum. A better control of this ultraviolet divergence is provided by the quantum link models [54,80,81] which still maintain exact gauge invariance using finite dimensional gauge links. We continue using the smallest dimensional representation for the $U(1)$ lattice gauge theory where the spin-$\frac{1}{2}$ operators are used for the gauge links as in the previous works [68,69]. The quantum links, as they are called, reside on the links $(r, \hat{\mu})$ connecting adjacent lattice sites r and $r + \hat{\mu}$. The electric flux operator is given by, $E_{r,\hat{\mu}} = S^3_{r,\hat{\mu}}$ and the gauge fields are raising (lowering) operators, $U_{r,\hat{\mu}}(U^\dagger_{r,\hat{\mu}}) = S^+_{r,\hat{\mu}}(S^-_{r,\hat{\mu}})$. The operator $\mathcal{O}_{\rm kin,\square}$ is composed of the elementary plaquette operator, $U_\square = U_{r,\hat{\mu}} U_{r+\hat{\mu},\hat{\nu}} U^\dagger_{r+\hat{\nu},\hat{\mu}} U^\dagger_{r,\hat{\nu}}$ and its hermitian conjugate $U^\dagger_\square$, which changes the direction of electric flux loops around an elementary plaquette (from clockwise to anticlockwise and vice versa) or annihilate nonflippable plaquettes. The other operator we will use in order to construct microscopic Hamiltonians in the following subsection is the operator $\mathcal{O}_{\rm pot,\square} = \mathbb{P}_{r,\hat{\mu},\uparrow}\mathbb{P}_{r+\hat{\mu},\hat{\nu},\uparrow}\mathbb{P}_{r+\hat{\nu},\hat{\mu},\downarrow}\mathbb{P}_{r,\hat{\nu},\downarrow} + \text{H.c.}$ $\mathbb{P}_{\uparrow(\downarrow)}$ is the projection operator to up (down) electric flux state of the gauge link. The structure of $\mathcal{O}_{\rm pot}$ counts the total number of flippable plaquettes: every flippable plaquette is counted as 1 irrespective of whether it is flippable in a clockwise or anticlockwise manner, but as 0 if not flippable. A pictorial representation of the actions of $\mathcal{O}_{\rm pot,\square}$ and $\mathcal{O}_{\rm kin,\square}$ on a plaquette is illustrated in the lower panel of Fig. 1. Note that the operators $\mathcal{O}_{\rm pot,\square}$ and $\mathcal{O}_{\rm kin,\square}$ use a four-body interaction, and the resulting theory is highly constrained: out of the 16 possible states at a single plaquette (for the spin-$\frac{1}{2}$ representation) states, only two are nontrivially acted up by the operators $\mathcal{O}_{\rm pot,\square}$ and $\mathcal{O}_{\rm kin,\square}$. It is also useful to recognize that for the spin-$\frac{1}{2}$ representation $\mathcal{O}_{\rm pot,\square} = \mathcal{O}^2_{\rm kin,\square}$, with higher powers of $\mathcal{O}_{\rm kin,\square}$ do not yield any new interactions which respect the gauge symmetry

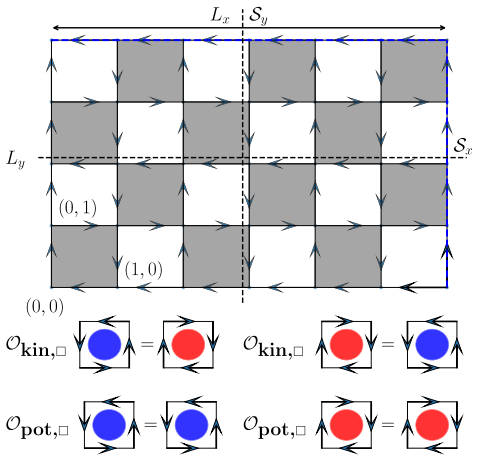

FIG. 1. Top panel: an electric flux configuration (an example Fock state) for a $(L_x, L_y) = (6, 4)$ lattice with periodic boundary condition in both directions. Even (odd) sublattice has been shown by shaded (blank) plaquettes. $\mathcal{S}_x$ $(\mathcal{S}_y)$ is the reflection operation about x (y) axis (shown by dotted lines). Bottom panel: action of $\mathcal{O}_{\rm kin,\square}$ and $\mathcal{O}_{\rm pot,\square}$ on elementary flippable plaquettes. An elementary plaquette flippable in the clockwise (anticlockwise) manner is shown by red (blue) circle.

(which will be discussed next). As such in the lattice gauge theory setup, this can be considered to be an adjoint interaction term for the gauge links. The other local interactions could be to take products of electric fields on the four links of the plaquette, but oriented in different fashion, but it is unclear what such interactions physically represent, and we do not consider such interactions in this work.

It is also useful to define the notion of a Fock state in the context of this model. In a quantum field theory, or a quantum many-body system, one typically starts from an empty state (which for example has no fermions, or in the case of spins, all spins pointing in a particular direction). Since our model has only spin-degrees of freedom, we could start from a state with all spins initialized to $S^z = -\frac{1}{2}$ and then apply creation operators to appropriate spins to get a desired Fock state. The resulting state is diagonal in the computational (electric flux) basis, and an example of such a state is represented in Fig. 1. Clearly, as in a typical many-body system, the system has exponentially many Fock states, however we only need to keep track of those not related by any symmetry.

The specific form of the Hamiltonians we build using the operators $\mathcal{O}_{\rm pot,\square}$, $\mathcal{O}_{\rm kin,\square}$ is explained in the next section, but before we discuss them, we consider the symmetries which are common to all the Hamiltonians considered in this article. The most relevant one is the local $U(1)$ symmetry, which arises due to the existence of the local operator,

$$G_r = \sum_\mu (E_{r,\hat{\mu}} - E_{r,r-\hat{\mu}}), \tag{1}$$

which commutes with both the operators $[G_r, \mathcal{O}_{\rm pot}] = 0$, $[G_r, \mathcal{O}_{\rm kin}] = 0$, and thus with all Hamiltonians which use these operators as building blocks. Moreover, note that the local operator is defined on the sites and for the square lattice, and thus has four links touching each site. Because of this commutation relations, the Hilbert space splits into exponentially many superselection sectors which then need to be specified by imposing the Gauss' law on particular states. We will give explicit examples when we discuss the model Hamiltonians.

Other symmetries of the Hamiltonians we will consider are all global. First, one has the discrete symmetries such as lattice translations, lattice rotations, reflections, elements of the point group symmetries of the square (rectangular) lattice. The presence or absence of some reflection symmetries will play a crucial role in our work. As an example, Fig. 1 (top panel), shows two particular reflection axes $\mathcal{S}_{x,y}$. Not all point-group symmetries commute with each other. Further, the Hamiltonians we consider are invariant to shifts by one lattice spacing, but one of the Hamiltonians we use will only be invariant by two lattice spacings. The charge conjugation $\mathbb{C}$ is another global symmetry, which transforms ${}^{\mathbb{C}}E_{r,\hat{\mu}} = -E_{r,\hat{\mu}}$, ${}^{\mathbb{C}}U_{r,\hat{\mu}} = U^{\dagger}_{r,\hat{\mu}}$, and ${}^{\mathbb{C}}U^{\dagger}_{r,\hat{\mu}} = U_{r,\hat{\mu}}$. Finally, the model has a global $U(1) \times U(1)$ winding number symmetry corresponding to each spatial direction, generated by the operator $W_\mu = \frac{1}{L_\mu}\sum_r E_{r,\hat{\mu}}$. For a detailed discussion of the symmetries, the reader is referred to Ref. [69]. We will, henceforth, focus on the largest sector with zero winding, i.e., $(W_x, W_y) = (0, 0)$.

A. Two $U(1)$ quantum link lattice gauge theories

The first model we consider is the one corresponding to the $U(1)$ quantum link model, whose Hamiltonian is given in terms of the plaquette operators introduced before, as follows:

$$\begin{aligned}\mathcal{H}_{\rm RK} &= \mathcal{O}_{\rm kin} + \lambda\mathcal{O}_{\rm pot} = -\sum_{\square}\mathcal{O}_{{\rm kin},\square} + \lambda\sum_{\square}\mathcal{O}_{{\rm pot},\square}, \\ &= -\sum_{\square}(U_\square + U^{\dagger}_\square) + \lambda\sum_{\square}(U_\square + U^{\dagger}_\square)^2. \end{aligned} \tag{2}$$

As noted previously, this Hamiltonian commutes with the Gauss law operator in Eq. (1). Different choices of the Gauss law decide different sectors, each with their own interesting physics. For example, demanding that the vacuum is free of any charge implies the definition of physical states to be $G_r|\psi\rangle = 0$, for all values of r. The physics in this sector is relevant for the physics of confining Abelian gauge theories [55], as well as that of quantum spin-ice [71,76]. Similarly, if one chooses the Gauss law sector which consists of static (heavy) charges which are distributed throughout the lattice with the even-parity sites having a charge $Q_r = +1$ and odd-parity sites having $Q_r = -1$, then the physics on the square lattice is that of the quantum dimer model, relevant in the theories of high-temperature superconductivity [58,70,74]. These models have a rich phase diagram consisting of fractionally charged electric strings [73] which break the translational symmetry and give rise to crystalline confined phases, which confine static charges at zero temperature. At finite temperatures, this model undergoes a phase transition into the deconfined phase, with the continuous phase transition lying in the 2D XY universality class. Instead of single charges, if one uses charges $Q_r = \pm 2$ which hop on the lattice due to thermal fluctuations alone, then the resulting finite temperature phase transition exhibits weak universality [82].

The second model we consider is very similar to the first Hamiltonian, except that the potential term carries a staggered coupling:

$$\begin{aligned}\mathcal{H}_{\rm st} &= -\sum_{\square}\mathcal{O}_{{\rm kin},\square} + \lambda\sum_{\square}(-1)^{\square}\mathcal{O}_{{\rm pot},\square}, \\ &= -\sum_{\square}(U_\square + U^{\dagger}_\square) + \lambda\sum_{\square}(-1)^{r_x+r_y}(U_\square + U^{\dagger}_\square)^2. \end{aligned} \tag{3}$$

Note that each plaquette here is labelled by the lower left site, and therefore the sign $(-1)^{\square} = (-1)^{r_x+r_y}$ is decided by whether the lower left site $r = (r_x, r_y)$ has even or odd parity.

We stress that while the Gauss law, the winding numbers and the charge conjugation are the same for both the models, point group symmetries like reflections and translations act differently due to the presence/absence of the staggered coupling; e.g., while the first Hamiltonian is translationally invariant by one lattice spacing in both $\hat{\mu} = \hat{x}, \hat{y}$, the second Hamiltonian is invariant to spatial translations by two lattice spacing due to the staggered couplings in $\mathcal{H}_{\rm st}$.

B. An index theorem and midspectrum zero modes

Both the models, $\mathcal{H}_{\rm RK}$ [Eq. (2)] and $\mathcal{H}_{\rm st}$ [Eq. (3)], are identical when $\lambda = 0$ and describe a nonintegrable $U(1)$ LGT [68,69]. The spectrum of $\mathcal{O}_{\rm kin}$ has a spectral reflection symmetry due to the presence of an operator $\mathcal{C}_\alpha$ (where $\alpha = x, y$) that anticommutes with $\mathcal{O}_{\rm kin}$, where

$$\mathcal{C}_\alpha = \prod_{r,\alpha} E_{r,\alpha}. \tag{4}$$

Only the horizontal links with even (odd) r_y [similarly, the vertical bonds with even (odd) r_x] contribute for $\alpha = x$ [similarly for $\alpha = y$] when $\frac{L_x}{2}$ is odd (even) [similarly, $\frac{L_y}{2}$ is odd (even)] in Eq. (4). For example, $\mathcal{C}_x$ is defined using the product of horizontal links on $\frac{L_y}{2} = 2$ alternate rows with odd values of r_y and $\mathcal{C}_y$ is defined using the product of vertical links on $\frac{L_x}{2} = 3$ alternate columns with even values of r_x for the (6,4) lattice depicted in Fig. 1. This definition

ensures that only one link in every elementary plaquette on the lattice contributes to $\mathcal{C}_\alpha$ from which it follows that

$$\{\mathcal{O}_{\text{kin}}, \mathcal{C}_\alpha\} = 0. \tag{5}$$

From the local constraint that $G_r|\psi\rangle = 0$ at each lattice point r, we obtain that $\mathcal{C}_x\mathcal{C}_y = 1$ implying that these are not independent of each other. For any eigenstate of $\mathcal{O}_{\text{kin}}$ with energy $E \neq 0$, denoted by $|E\rangle$, there exists another eigenstate $\mathcal{C}_\alpha|E\rangle$ (where α may be chosen to be x or y) with energy $-E$.

$\mathcal{O}_{\text{kin}}$ commutes with the space reflection symmetries defined along the horizontal (S_x) or vertical (S_y) axis (see Fig. 1) which divides the lattice in two equal halves leading to

$$[\mathcal{O}_{\text{kin}}, S_\alpha] = 0 \tag{6}$$

for $\alpha = x, y$. Furthermore, in defining $\mathcal{C}_x$ and $\mathcal{C}_y$, the $\frac{L_y}{2}$ rows and the $\frac{L_x}{2}$ columns containing the links are located symmetrically with respect to the reflection axes S_x and S_y resulting in $\mathcal{C}_\alpha$ commuting with both S_x and S_y, irrespective of α, yielding

$$[\mathcal{C}_\alpha, S_\beta] = 0 \tag{7}$$

for $\alpha, \beta = x, y$.

Remarkably, any Hamiltonian with these properties [Eqs. (5)–(7)] has exact zero energy eigenstates with $E = 0$ whose number scales exponentially with system size but which are, nonetheless, protected due to an index theorem as discussed in Refs. [22,23,77]. Following these references, one can also show that the number of zero modes is bounded below by $\sqrt{\text{HSD}}$, where HSD denotes the total Hilbert space dimension for a spin-$\frac{1}{2}$ QLM in a (L_x, L_y) ladder in the appropriate winding number sector [zero winding number sector $(W_x, W_y) = (0, 0)$ in our case]. These zero modes of $\mathcal{O}_{\text{kin}}$ turn out to be the only eigenstates that have a well-defined "chiral charge" of ± 1 under the action of $\mathcal{C}_\alpha$ with $\alpha = x, y$ distinguishing them from all the nonzero modes of $\mathcal{O}_{\text{kin}}$ which are not eigenstates of $\mathcal{C}_\alpha$.

The number of zero modes for $\mathcal{O}_{\text{kin}}$ for a range of (L_x, L_y) lattices that can be extracted from ED is shown in Table I. Table I also shows the HSD for these lattices from exact enumeration.

It is useful to ask whether the index theorem is preserved when noncommuting terms like $\sum_\square \mathcal{O}_{\text{pot},\square}$ or $\sum_\square (-1)^\square \mathcal{O}_{\text{pot},\square}$ are added to $\mathcal{O}_{\text{kin}}$. It turns out that adding $\sum_\square \mathcal{O}_{\text{pot},\square}$ immediately violates the index theorem since an appropriate chiral operator which anticommutes with $\mathcal{H}_{\text{RK}}$ cannot be constructed unless $\lambda = 0$, making the spectrum lose its $E \to -E$ symmetry for $\lambda \neq 0$. On the other hand, adding the $\sum_\square (-1)^\square \mathcal{O}_{\text{pot},\square}$ to $\mathcal{O}_{\text{kin}}$ as done in $\mathcal{H}_{\text{st}}$ presents an interesting case where the index theorem can be preserved for any λ. This is because while $\sum_\square (-1)^\square \mathcal{O}_{\text{pot},\square}$ commutes with $\mathcal{C}_\alpha$ (for $\alpha = x, y$), it anticommutes with both S_x and S_y unlike $\sum_\square \mathcal{O}_{\text{pot},\square}$, which commutes with S_x and S_y. This allows for the weaker condition of $\{\mathcal{H}_{\text{st}}, \mathcal{C}_\alpha S_\beta\} = 0$ for $\alpha, \beta = x, y$ to be satisfied for any λ which turns out to be sufficient to ensure the index theorem as demonstrated in Ref. [23]. In fact, the number of zero modes of $\mathcal{H}_{\text{st}}$ for a (L_x, L_y) lattice stays unchanged for any $\lambda \in (0, \infty)$ and is given in Table I. Note that it does not imply that the zero modes themselves stay unchanged as a function of λ. Figure 2 shows the scaling of the number of zero modes of $\mathcal{O}_{\text{kin}}$ and $\mathcal{H}_{\text{st}}$, respectively, and $\sqrt{\text{HSD}}$ on various $(L_x, 2)$ ladders to explicitly demonstrate the validity of the index theorem as well as the accuracy of the lower bound on the number of the zero modes.

TABLE I. Number of midspectrum zero modes in $\mathcal{O}_{\text{kin}}$ and $\mathcal{H}_{\text{st}}$ and the HSD for various lattices.

$L_x \times L_y$	Zero modes in $\mathcal{O}_{\text{kin}}$	Zero modes in $\mathcal{H}_{\text{st}}$	HSD
6×2	34	30	282
8×2	178	94	2214
10×2	346	294	17906
12×2	1658	886	147578
4×4	158	74	990
6×4	1070	426	32810

III. SUBLATTICE SCARS

References [68,69] discussed high-energy eigenstates of $\mathcal{H}_{\text{RK}}$ [Eq. (2)] for (L_x, L_y) lattices with periodic boundary conditions in both directions that stayed unchanged as a function of λ by virtue of being simultaneous eigenstates of both $\mathcal{O}_{\text{kin}}$ and $\mathcal{O}_{\text{pot}}$. The fact that these high-energy states do not mix with the exponentially large (in system size)

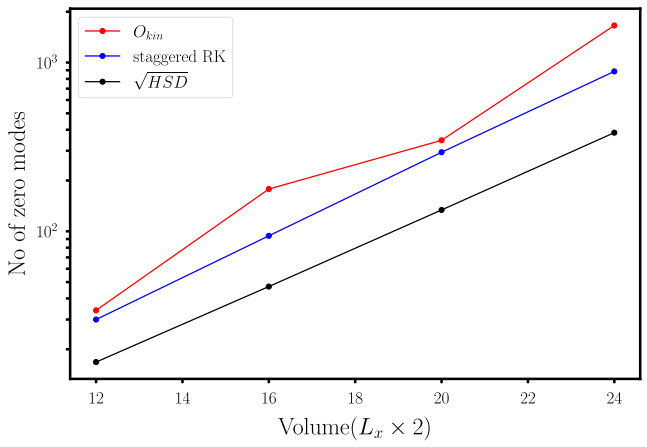

FIG. 2. Scaling of the number of midspectrum zero modes with system size in two models which satisfy index theorem. The behaviour of the lower bound $\sqrt{\text{HSD}}$ is also shown.

number of neighboring high-energy states as λ is varied, immediately implies a violation of the ETH [68]. A class of these eigenstates have $\mathcal{O}_{\rm pot} = \frac{N_p}{2}$ (where $N_p = L_x L_y$ refers to the number of elementary plaquettes) and $\mathcal{O}_{\rm kin} = 0$ or ± 2 as ED studies of Refs. [68,69] showed. However, an analytic understanding of these scars in the QLM was lacking so far. We will give a physical description of these scars in what follows below, which will also demonstrate their existence in 2D lattices.

It turns out that scars with $(\mathcal{O}_{\rm kin}, \mathcal{O}_{\rm pot}) = (0, \frac{N_p}{2})$ and $(\pm 2, \frac{N_p}{2})$ have much more structure than being just eigenstates of $\mathcal{O}_{\rm pot}$. All such scars for the finite lattices analyzed in Ref. [69] can be understood from the following ansatz that the scar states $|\psi_s\rangle$ satisfy $\mathcal{O}_{{\rm pot},\square}|\psi_s\rangle = |\psi_s\rangle$ for one sublattice and $\mathcal{O}_{{\rm pot},\square}|\psi_s\rangle = 0$ for the other sublattice (where there are two equivalent choices of which sublattice has $\mathcal{O}_{{\rm pot},\square}|\psi_s\rangle = |\psi_s\rangle$). Since these sublattice scars are midspectrum eigenstates of a nonintegrable theory [69], namely $\mathcal{O}_{\rm kin}$, ETH would have predicted $\mathcal{O}_{{\rm pot},\square}|\psi_s\rangle = \frac{1}{2}|\psi_s\rangle$, independent of which sublattice an elementary plaquette is located. Thus, these sublattice scars clearly violate ETH. We will discuss a class of sublattice scars that have a description in terms of emergent short singlets on an appropriately defined dual square lattice in Sec. III A and will also place a lower bound on the number of these scars for arbitrary (even) (L_x, L_y) lattices. Not all sublattice scars have such an analytic description and these nonsinglet scars will be discussed in Secs. III B and III C. The understanding of the structure of these nonsinglet scars was greatly helped by an efficient numerical algorithm to specifically target sublattice scars (but not the full Hilbert space) and would be discussed in the next section.

A. Short singlet sublattice scars

A class of sublattice scars with $\mathcal{O}_{\rm kin} = 0$ can be constructed exactly using a tiling representation in terms of emergent singlets. Let us denote the plaquettes with $\mathcal{O}_{{\rm pot},\square} = 1$ ($\mathcal{O}_{{\rm pot},\square} = 0$) as active (inactive). For sublattice scars, any active plaquette is surrounded by four inactive plaquettes as its nearest neighbors (sharing a common link) and vice versa. Now, consider two nearest neighbor active plaquettes that share a common vertex. These plaquettes can only have the following four local configurations, (C, A), (A, C), (C, C), and (A, A), where C (A) denotes an elementary plaquette where the electric fluxes have a clockwise (anticlockwise) circulation. The inactive plaquettes on the other sublattice are denoted by U henceforth. It is important to stress here that $\mathcal{O}_{{\rm pot},\square} = 0$ on a plaquette does not fix its electric flux configuration and allows for electric flux fluctuations since there are 14 local flux configurations that are U on any elementary plaquette.

Let us first consider two nearest neighbor active plaquettes that are either in the local configuration (A, C) or (C, A). This automatically ensures that the two plaquettes on the other sublattice that share edges with both these active plaquettes are U without the need of specifying the electric fluxes on any other links of these plaquettes. The above statement is not true if the local configuration of two nearest neighbor active plaquettes is either (A, A) or (C, C) and enforces extra constraints on the state of the other active plaquettes that are in contact with the two U plaquettes to ensure their unflippability. We can now take this 2×2 unit of two flippable and two unflippable plaquettes and apply $\mathcal{O}_{\rm kin}$ on this unit. This gives a configuration as shown in Figs. 3(a), 3(b) from which it is clear that acting $\mathcal{O}_{\rm kin}$ on a singlet of $\frac{1}{\sqrt{2}}$(A, C − C, A) annihilates the state [Fig. 3(c)].

We now ask whether these 2×2 units comprising a singlet and two unflippable plaquettes can be used to tile the entire (L_x, L_y) lattice and give sublattice scars. We define a dual square lattice by joining the centers of the active plaquettes on one sublattice [Fig. 4(a)]. The emergent singlets can be thought of as living on the bonds of this dual lattice. These singlets naturally act as hard-core dimers because any active plaquette cannot be part of more than one singlet. Furthermore, the perpendicular bisector of each such dimer touches the center of the two unflippable plaquettes in the 2×2 unit [Fig. 4(a)]. Since the number of unflippable plaquettes equals $\frac{N_p}{2}$, none of these perpendicular bisectors associated with the hard-core dimers (representing the singlets) can share ends and thus act as dual dimers with their own hard-core repulsion on the square lattice defined by bonds touching the centers of the inactive plaquettes. The allowed coverings of these dimers

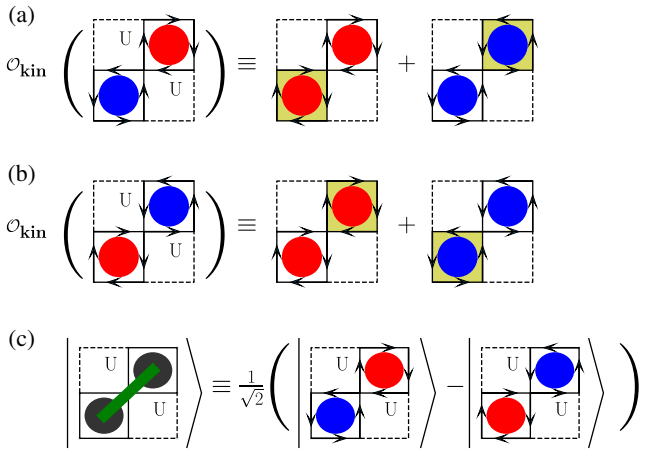

FIG. 3. (a) and (b) show the action of $\mathcal{O}_{\rm kin}$ on two 2×2 units composed of two unflippable plaquettes and one clockwise and one anticlockwise flippable plaquette. Clockwise (anticlockwise) circulation of electric fluxes on a plaquette is shown by a red (blue) circle as in Fig. 1. The plaquette marked by a yellow background indicates the one on which $\mathcal{O}_{\rm kin}$ acts in panels (a) and (b). (c) Representation of an emergent singlet in the same 2×2 unit.

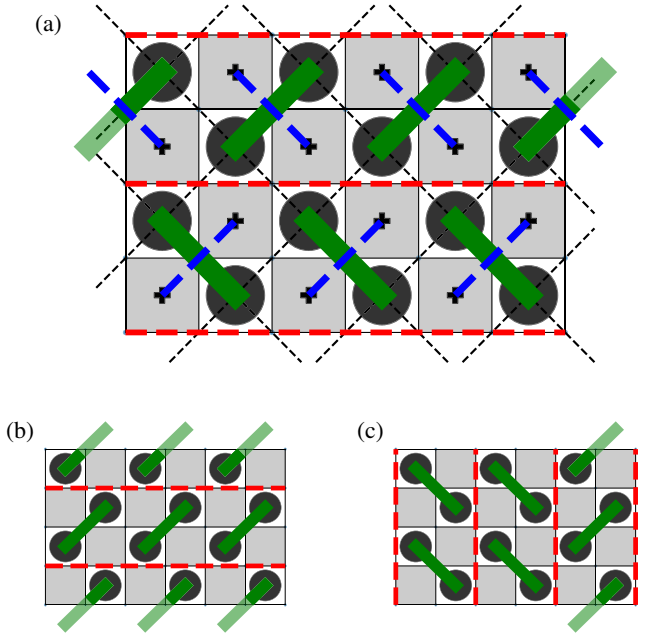

FIG. 4. Graphical representations of some short singlet sublattice scars for a (6,4) lattice. The white (gray) plaquettes in all panels denote active (inactive) plaquettes with $\mathcal{O}_{\mathrm{pot},\square} = 1(0)$. The singlets (or dimers), shown as thick green lines, follow the same convention as shown in Fig. 3(c) and reside on the bonds of the dual square lattice formed by connecting the centers of the active plaquettes as indicated in panel (a) by thin dotted lines. Each dimer has an associated perpendicular bisector as shown in panel (a) by dotted blue lines. Panels (a) and (b) show two horizontal partitions of width 2 while panel (c) shows three vertical partitions of width 2 using dotted red lines.

(i.e., singlets) and their associated perpendicular bisectors (the dual dimers) define all sublattice scars with a simple emergent singlet description. Each of these short singlet sublattice scars are eigenstates of $\mathcal{O}_{\mathrm{kin}}$ with eigenvalue 0 and satisfy $\mathcal{O}_{\mathrm{pot},\square}|\psi\rangle = c|\psi\rangle$, where $c = 1$ (0) for the active (inactive) elementary plaquettes.

Let us now discuss the degeneracy of such singlet sublattice scars on (L_x, L_y) lattices. Consider the $(L_x, 2)$ ladder first, and focus on active plaquettes on one particular sublattice. It can be seen that the hard-core constraints on the singlets and their associated perpendicular bisectors only allow for two possible coverings such that all short singlets are parallel to each other with their possible alignment providing the additional degeneracy of 2. Since the choice of active plaquettes on one sublattice is arbitrary, the total number of such short singlet sublattice scars equals $2 + 2 = 4$ for $(L_x, 2)$ ladders.

We next consider the degeneracy of short singlet sublattice scars for wider ladders with $(L_x, 4)$. The valid dimer coverings can be constructed by first dividing the lattice into a close packing of parallel nonoverlapping horizontal or vertical partitions (see Fig. 4 for some examples), each of width 2, and then arranging parallel dimers in each partition in one of the two possible orientations. The internal orientation of the parallel dimers can be assigned in each of the partitions independently. For $(L_x, 4)$ lattices, there are two ways to divide the lattice into $\frac{4}{2} = 2$ $(\frac{L_x}{2})$ nonoverlapping horizontal (vertical) partitions taking into account periodic boundary conditions. This gives the total number of dimer coverings to be $(8 + 2^{\frac{L_x}{2}+1})$ out of which four dimer coverings that comprise all dimers being parallel to each other are repeated by multiple partitions. Thus, the total number of distinct dimer coverings on one particular sublattice of active plaquettes equals $(8 + 2^{\frac{L_x}{2}+1} - 4)$. Not all these dimer coverings are linearly independent states. An explicit calculation shows that For a (4,4) lattice, 10 out of 12 such dimer coverings are linearly independent scars while the number appears to be $(3 + 2^{\frac{L_x}{2}+1})$ for $L_x > 4$ (see Table II). Extending this counting to an arbitrary (L_x, L_y) lattice, we thus obtain $\mathcal{O}(2^{\frac{L_x}{2}+1} + 2^{\frac{L_y}{2}+1} - 4)$ such short singlet sublattice scars that immediately provides a lower bound on the number of sublattice scars.

Let us briefly discuss the symmetries of these scars. While the short singlet sublattice scars do not, in general, have a well-defined momentum since the dimer covering may not have any particular periodicity, all these states are eigenstates of the charge conjugation $\mathbb{C}$. Since the emergent singlet is odd under $\mathbb{C}$, a short singlet scar composed of even (odd) number of singlets has $\mathbb{C} = +1$ (-1). Since one needs $\frac{L_x L_y}{4}$ short singlets to form a sublattice scar, these particular scars have $\mathbb{C} = (-1)^{\frac{L_x L_y}{4}}$ for a (L_x, L_y) lattice.

B. Nonsinglet sublattice scars

From our numerical algorithm that explicitly targets sublattice scars (see Sec. IV for a discussion of the procedure), we can compute the total number of sublattice scars in finite (L_x, L_y) lattices. This information is given in Table II for sublattice scars with $\mathcal{O}_{\mathrm{kin}} = 0$ where the active plaquettes (with $\mathcal{O}_{\mathrm{pot},\square} = 1$) have been chosen to be on one

TABLE II. Number of sublattice scars with $\mathcal{O}_{\mathrm{kin}} = 0$ in one sublattice for various lattices. The sublattice scars can be further classified into short singlet scars, nonsinglet scars formed out of Fock states with an equal (unequal) number of clockwise (represented by C) and anticlockwise (represented by A) flippable active plaquettes. The corresponding degeneracies have been separately listed for clarity.

	Scars in equal A-C sector		Scars in unequal A-C sector
Lattice	Singlet scars	Nonsinglet scars	
$L_x \times 2$	2	0	0
4×4	10	0	3
6×4	19	3	1
8×4	35	17	1
10×4	67	62	1
6×6	28	1	1

particular sublattice. While all sublattice scars for $L_y = 2$ turn out to be short singlet scars, wider lattices with $L_y \geq 4$ immediately lead to the presence of nonsinglet sublattice scars. From explicit calculations, we see that sublattice scars with $\mathcal{O}_{\text{kin}} = 0$ can be written as a linear combination of Fock states that involve either $(\frac{N_p}{4}, \frac{N_p}{4})$ ($\boxed{\text{A}}$,$\boxed{\text{C}}$) or $(\frac{N_p}{4} \pm 1, \frac{N_p}{4} \mp 1)$ ($\boxed{\text{A}}$,$\boxed{\text{C}}$) active plaquettes (Table II). The above notation indicates the number of anticlockwise and clockwise plaquettes in each of the Fock states that contribute to the scars. Clearly, short singlet scars belong to the former variety while the latter variety cannot have a short singlet representation. Focusing on sublattice scars that can be expressed as a linear combination of Fock states with $(\frac{N_p}{4}, \frac{N_p}{4})$ ($\boxed{\text{A}}$,$\boxed{\text{C}}$) active plaquettes, we see that while (4, 4) lattice does not have any nonsinglet scar, $L_x \geq 6$ for $L_y = 4$ has several nonsinglet scars whose number seems to rapidly increase with L_x. It is not clear to us whether this number in fact exceeds the corresponding number of singlet scars when $L_x > 10$ for $L_y = 4$. For (6, 6) there is exactly 1 such nonsinglet scar but we expect that this number again increases as $L_x > 6$ for $L_y = 6$. Note that accessing even (10, 4) lattices with ED targeting the full Hilbert space is extremely resource intensive and here we have used the algorithm presented in Sec. IV.

We now come to the sublattice scars that can be expressed in terms of Fock states with $(\frac{N_p}{4} + 1, \frac{N_p}{4} - 1)$ and $(\frac{N_p}{4} - 1, \frac{N_p}{4} + 1)$ ($\boxed{\text{A}}$,$\boxed{\text{C}}$) active plaquettes on one particular sublattice. Interestingly, their number does not seem to increase with lattice dimension unlike the singlet and nonsinglet scars composed of an equal number of clockwise and anticlockwise active plaquettes (Table II). While there are three such sublattice scars for a (4, 4) lattice, there is only one such scar for (6, 4), (8, 4), (10, 4), and (6, 6) lattices. A particular linear combination of the three sublattice scars (which is also a sublattice scar, by definition) for a (4, 4) lattice is shown in Fig. 5. This scar has the property that all the Fock states that combine to form this state contribute with equal magnitudes but with an intricate sign structure as depicted in Fig. 5, and the state can be expressed as

$$|\psi_{s,0}\rangle = \frac{1}{2\sqrt{6}} \sum_{i=1}^{12} \text{Sign}(i)(|F_i\rangle + \mathbb{C}|F_i\rangle), \tag{8}$$

where we refer the reader to Fig. 5 for Sign(i) for the corresponding $|F_i\rangle$. This striking property of the amplitudes of the contributing Fock states turns out to be true for the unique scar with $(\frac{N_p}{4} + 1, \frac{N_p}{4} - 1)$ and $(\frac{N_p}{4} - 1, \frac{N_p}{4} + 1)$ ($\boxed{\text{A}}$,$\boxed{\text{C}}$) active plaquettes on one particular sublattice for bigger lattices than (4, 4).

We comment on the symmetries of the nonsinglet scars. We observe that the eigenvalues of the operator $\mathbb{C}$ for these

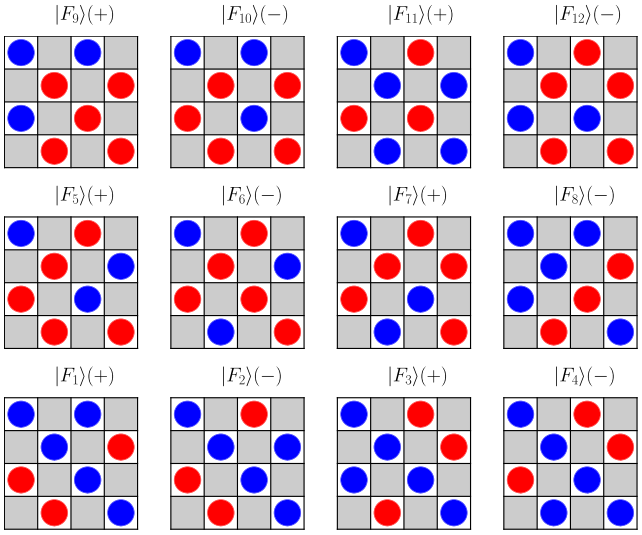

FIG. 5. One of the three sublattice scars with $\mathcal{O}_{\text{kin}} = 0$ and having contributions from unequal number of clockwise and anticlockwise flippable plaquettes for 4×4 lattice. Clockwise (anticlockwise) circulation of electric fluxes on a plaquette is shown by a red (blue) circle as in Fig. 1. The white (gray) plaquettes denote active (inactive) plaquettes with $\mathcal{O}_{\text{pot},\square} = 1(0)$ as in Fig. 4.

states are $(-1)^{\frac{L_x L_y}{4}}$, just like the short singlet scars, though we do not have an analytic proof in this case. Second, the unique scars formed by combining Fock states with $(\frac{N_p}{4} + 1, \frac{N_p}{4} - 1)$ and $(\frac{N_p}{4} - 1, \frac{N_p}{4} + 1)$ ($\boxed{\text{A}}$,$\boxed{\text{C}}$) active plaquettes on one particular sublattice for (6, 4),(8, 4),(10, 4), and (6, 6) lattices have a well-defined momentum with respect to translations by two lattice units in both directions $\hat{x}$ and $\hat{y}$ (the sublattice structure rules out any symmetry of these states with respect to translations by one lattice unit). We denote the momentum as $\hat{k}_x, \hat{k}_y$ to avoid any confusion with the usual momentum, defined through single lattice translations. While these scars for (6, 4),(8, 4),(10, 4) lattices have a momentum $(\hat{k}_x, \hat{k}_y) = (0, 0)$, the scar for the (6, 6) lattice is at momentum $(\hat{k}_x, \hat{k}_y) = (\pi, \pi)$. The unique nonsinglet scar for a (6,6) lattice that involves equal number of clockwise and anticlockwise plaquettes on one sublattice also carries a momentum $(\hat{k}_x, \hat{k}_y) = (\pi, \pi)$.

One can ask how the local operators differ in any nonsinglet scar compared to any short singlet scar. These operators must be other than $\mathcal{O}_{\text{pot},\square}$ which cannot distinguish between the two cases. However, certain two-plaquette correlation functions, where the two plaquettes are nearest neighbor active plaquettes sharing a common vertex, are sensitive to the scar states. We expect that these operators can be measured straightforwardly in quantum simulator experiments, and provide a route to the experimental demonstration of these states. The four-dimensional

local Hilbert space can then be represented in terms of singlets and triplets in the following manner:

$$|t_{+1}\rangle = (\boxed{\text{A}}, \boxed{\text{A}}),$$
$$|t_{-1}\rangle = (\boxed{\text{C}}, \boxed{\text{C}}),$$
$$|t_0\rangle = \frac{1}{\sqrt{2}}(\boxed{\text{A}}, \boxed{\text{C}} + \boxed{\text{C}}, \boxed{\text{A}}),$$
$$|s_0\rangle = \frac{1}{\sqrt{2}}(\boxed{\text{A}}, \boxed{\text{C}} - \boxed{\text{C}}, \boxed{\text{A}}). \quad (9)$$

We can then probe the expectation values of the operators $|t_{\pm1,0}\rangle\langle t_{\pm1,0}|$ and $|s_0\rangle\langle s_0|$ locally for all nearest neighbor active plaquettes given any sublattice scar, which we denote by a shorthand $\langle t_{\pm1,0}\rangle_{(r_1,r_2)}$, $\langle s_0\rangle_{(r_1,r_2)}$, where (r_1, r_2) indicates the bond connecting the centers of the two plaquettes. For a short singlet sublattice scar, $\langle s_0\rangle_{(r_1,r_2)} = 1$ and $\langle t_{\pm1,0}\rangle_{(r_1,r_2)} = 0$ for the bonds that carry a singlet (dimer) (Fig. 4) and $\langle t_{\pm1,0}\rangle_{(r_1,r_2)} = \langle s_0\rangle_{r_1,r_2} = \frac{1}{4}$ for the other bonds (Fig. 4). For nonsinglet sublattice scars, we choose to probe these local operators for both the unique nonsinglet sublattice scar with equal number of clockwise and anticlockwise active plaquettes [Fig. 6(a)] and with $(\frac{N_p}{4} \pm 1, \frac{N_p}{4} \mp 1)$ clockwise and anticlockwise active plaquettes [Fig. 6(b)] on a (6, 6) lattice. For both these nonsinglet scars, the values of $\langle t_{\pm1,0}\rangle_{(r_1,r_2)}$, and $\langle s_0\rangle_{(r_1,r_2)}$ are independent of the location of the bond (r_1, r_2) and are quite different from short singlet scars. Probing these operators locally for the unique nonsinglet scar with $(\frac{N_p}{4} \pm 1, N_p \mp 1)$ clockwise and anticlockwise active plaquettes for $(L_x, 4)$ lattices with $L_x \geq 6$ again gives values of $\langle t_{\pm1,0}\rangle_{(r_1,r_2)}$, and $\langle s_0\rangle_{(r_1,r_2)}$ that are independent of the location of the bond (r_1, r_2). We obtain $\langle t_{\pm1}\rangle_{(r_1,r_2)} = \frac{1}{4}$ for $L_x = 6$, 8, 10, respectively, $\langle t_0\rangle_{(r_1,r_2)}(\langle s_0\rangle_{(r_1,r_2)}) \approx 0.2038(0.29167)$ for $L_x = 6$, $\langle t_0\rangle_{(r_1,r_2)}(\langle s_0\rangle_{(r_1,r_2)}) \approx 0.2187(0.2812)$ for $L_x = 8$ and $\langle t_0\rangle_{(r_1,r_2)}(\langle s_0\rangle_{(r_1,r_2)}) \approx 0.225(0.275)$ for $L_x = 10$.

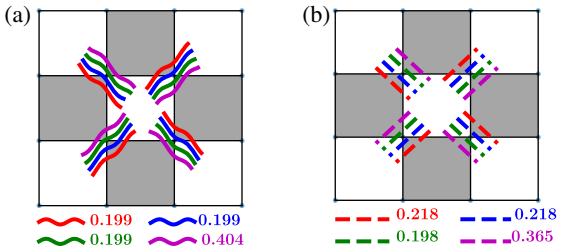

FIG. 6. Expectation value $\langle t_{+1}\rangle_{(r_1,r_2)}$ (red lines), $\langle t_{-1}\rangle_{(r_1,r_2)}$ (blue lines), $\langle t_0\rangle_{(r_1,r_2)}$ (green lines), and $\langle s_0\rangle_{r_1,r_2}$ (magenta lines) for the unique nonsinglet scars on a (6,6) lattice composed of (a) equal number of clockwise and anticlockwise active plaquettes, and (b) unequal number of clockwise and anticlockwise active plaquettes. The white (gray) plaquettes denote active (inactive) plaquettes with $\mathcal{O}_{\text{pot},\square} = 1(0)$ as in Fig. 4.

C. Sublattice scars with $\mathcal{O}_{\text{kin}} = \pm 2$

We also find sublattice scars with $\mathcal{O}_{\text{kin}} = \pm 2$ for systems with $L_y \geq 4$ (see Table III) that are simultaneous eigenstates of $\mathcal{O}_{\text{pot},\square}$ with it being equal to 1 on one sublattice and 0 on another. Since these states have nonzero integer values of $\mathcal{O}_{\text{kin}}$, these necessarily violate the ETH as a generic high-energy state would instead have an irrational energy eigenvalue. It is interesting to ask how such simple eigenvalues may be generated from $\mathcal{O}_{\text{kin}}$ since there is no analogous index theorem that ensures the presence of specific $E \neq 0$ eigenstates with such simple energies. Comparing Tables II and III, it is striking that the degeneracy of sublattice scars with $\mathcal{O}_{\text{kin}} = +2(-2)$ equals that of sublattice scars with $\mathcal{O}_{\text{kin}} = 0$ that are composed of Fock states with unequal number of clockwise and anticlockwise active plaquettes.

We now demonstrate a "triangle relation" between sublattice scars with $\mathcal{O}_{\text{kin}} = \pm 2$ and the sublattice scars with $\mathcal{O}_{\text{kin}} = 0$, composed of Fock states with $(\frac{N_p}{4} \pm 1, \frac{N_p}{4} \mp 1)$ clockwise and anticlockwise active plaquettes. For this, we note that the sublattice scars with $\mathcal{O}_{\text{kin}} = +2(-2)$ consist of both Fock states with $(\frac{N_p}{4}, \frac{N_p}{4})$ and $(\frac{N_p}{4} \pm 1, \frac{N_p}{4} \mp 1)$ clockwise and anticlockwise active plaquettes. Given any $|\psi_{s,+2}\rangle$ (where $+2$ denotes the $\mathcal{O}_{\text{kin}} = +2$ states), applying the chirality operator $\mathcal{C}_\alpha|\psi_{s,+2}\rangle$ generates a unique $|\psi_{s,-2}\rangle$ with $\mathcal{O}_{\text{kin}} = -2$ (α can be chosen to be x or y). Applying $\mathcal{C}_\alpha$ on the Fock states with $(\frac{N_p}{4}, \frac{N_p}{4})$ $[(\frac{N_p}{4} \pm 1, \frac{N_p}{4} \mp 1)]$ clockwise and anticlockwise active plaquettes gives an eigenvalue of $+1$ $[-1]$. Thus, $(|\psi_{s,+2}\rangle - \mathcal{C}_\alpha|\psi_{s,+2}\rangle)$ leads to a state with only Fock states with $(\frac{N_p}{4} \pm 1, \frac{N_p}{4} \mp 1)$ clockwise and anticlockwise active plaquettes contributing to it. These Fock states turn out to be identical to the ones that make up the sublattice scars with $\mathcal{O}_{\text{kin}} = 0$, and unequal number of clockwise and anticlockwise active plaquettes, but the sign structure of the states are nonetheless different.

We now define an operator $\mathcal{O}$ that acts on Fock states with $(\frac{N_p}{4} \pm 1, \frac{N_p}{4} \mp 1)$ clockwise and anticlockwise active plaquettes and leads to a sign change (no sign change) for Fock states with $(\frac{N_p}{4} + 1, \frac{N_p}{4} - 1)$ $((\frac{N_p}{4} - 1, \frac{N_p}{4} + 1))$ clockwise and anticlockwise active plaquettes. We then see that

$$\mathcal{O}(|\psi_{s,+2}\rangle - \mathcal{C}_\alpha|\psi_{s,+2}\rangle) \propto |\psi_{s,0}\rangle, \quad (10)$$

TABLE III. Number of sublattice scars with $\mathcal{O}_{\text{kin}} = \pm 2$ for various lattice dimensions.

Lattice	Scars with $\mathcal{O}_{\text{kin}} = +2$	Scars with $\mathcal{O}_{\text{kin}} = -2$
4×4	3	3
6×4	1	1
8×4	1	1
6×6	1	1

where $|\psi_{s,0}\rangle$ is a sublattice scar with $\mathcal{O}_{\rm kin}=0$ composed of Fock states with unequal number of clockwise and anticlockwise active plaquettes on one sublattice. We note that this relation is also true for (4,4) system where there is a threefold degeneracy of sublattice scars with $\mathcal{O}_{\rm kin}=+2(-2)$. We conjecture that such a "triangle relation" exists for all (L_x,L_y) lattices with $L_y\geq 4$.

Before closing this section, we note that sublattice scars with $\mathcal{O}_{\rm kin}=+2(-2)$ are eigenstates of charge conjugation with $\mathbb{C}=-1$ for (L_x,L_y) lattices with $L_y=4$ and with $\mathbb{C}=+1$ for (6, 6) lattice. Additionally, the unique sublattice scars with $\mathcal{O}_{\rm kin}=+2(-2)$ for (6, 4), (8, 4), and (6, 6) lattices have a well-defined momentum of $(\hat{k}_x,\hat{k}_y)=(0,0)$ with respect to translations by two lattice units on both directions.

IV. EFFICIENT ALGORITHM TO GENERATE SUBLATTICE SCARS

In this section, we discuss the efficient numerical procedure to specifically target the sublattice scars, unlike exact diagonalization, which constructs all states in the full Hilbert space. While both algorithms are computationally exponentially expensive, the former diverges slower, as can be guessed from Table I, and will be demonstrated further in Table IV. For this, we start with a set of n Fock states $\{|f_i\rangle\}_n$ that have the requisite sublattice structure, i.e., all plaquettes on one (other) sublattice are flippable (nonflippable). We will soon come to the question of how to generate this set efficiently. Our task is to now find states of the form $|\psi_s\rangle=\sum_{i=1}^n a_i|f_i\rangle$ such that $\mathcal{O}_{\rm kin}|\psi_s\rangle=\mathcal{N}|\psi_s\rangle$, where $\mathcal{N}$ is either zero or a nonzero integer. Given $\{|f_i\rangle\}_n$, we define a set of m Fock states $\{|F_i\rangle\}_m$, which contains all possible states generated by a single action of $\mathcal{O}_{\rm kin}$ on the set $\{|f_i\rangle\}_n$. This set can be written as $\{|F_i\rangle\}_m=\{|f_i\rangle\}_n+\{|f_i'\rangle\}_{m'}$, where $\{|f_i'\rangle\}_{m'}$ contains Fock states which do not have the sublattice structure of all flippable (nonflippable) plaquettes on one (other) sublattice. One can write $\mathcal{O}_{\rm kin}|f_i\rangle=\sum_{j=1}^m V_{ji}|F_j\rangle=\sum_{j=1}^n v_{ji}|f_j\rangle+\sum_{j=1}^{m'} v'_{ji}|f'_j\rangle$, where $V_{ji}=\langle F_j|\mathcal{O}_{\rm kin}|f_i\rangle$, $v_{ji}=\langle f_j|\mathcal{O}_{\rm kin}|f_i\rangle$, and $v'_{ji}=\langle f'_j|\mathcal{O}_{\rm kin}|f_i\rangle$.

First, we consider the sublattice scars with $\mathcal{O}_{\rm kin}|\psi_s\rangle=0$. We then have $\mathcal{O}_{\rm kin}|\psi_s\rangle=\sum_{i=1}^n a_i\sum_{j=1}^m V_{ji}|F_j\rangle=\sum_{j=1}^m(\sum_{i=1}^n V_{ji}a_i)|F_j\rangle$. To satisfy $\mathcal{O}_{\rm kin}|\psi_s\rangle=0$, we need to satisfy m simultaneous conditions: $\sum_{i=1}^n V_{ji}a_i=0$ for $j=1$ to m. The possible set of solutions $(\{a_i\})$ specify the sublattice scars with $\mathcal{O}_{\rm kin}=0$. For this, we construct the $m\times n$ dimensional matrix $[\mathbb{V}_{m\times n}]_{ji}=v_{ji}$. If we perform a singular value decomposition of $\mathbb{V}$, then the right-singular vectors $(\{[\Phi_{n\times 1}]\})$ with zero-singular value satisfy the above conditions because $[\mathbb{V}_{m\times n}][\Phi_{n\times 1}]=[\varnothing_{m\times 1}]\Rightarrow\sum_{i=1}^n V_{ji}[\Phi_{n\times 1}]_{i1}=0$ for $j=1$ to m. These right-singular vectors are then the required sublattice scars with $\mathcal{N}=0$.

Next, we consider the sublattice scars with $\mathcal{O}_{\rm kin}|\psi_s\rangle=\mathcal{N}|\psi_s\rangle$, where $\mathcal{N}$ is a nonzero integer. This requires a more complicated procedure. We can write $\mathcal{O}_{\rm kin}|\psi_s\rangle=\sum_{j=1}^n(\sum_{i=1}^n v_{ji}a_i)|f_j\rangle+\sum_{j=1}^{m'}(\sum_{i=1}^n v'_{ji}a_i)|f'_j\rangle$. To satisfy $\mathcal{O}_{\rm kin}|\psi_s\rangle=\mathcal{N}|\psi_s\rangle$ with $\mathcal{N}\neq 0$, we need to satisfy two conditions simultaneously: (i) $\sum_{i=1}^n v_{ji}a_i=\mathcal{N}a_j$ for $j=1$ to n and (ii) $\sum_{i=1}^n v'_{ji}a_i=0$ for $j=1$ to m'. First, we construct the matrix $[\mathbb{V}'_{m'\times n}]_{ji}=v'_{ji}$. As we have already argued before, the right-singular vectors of $\mathbb{V}'$ with zero-singular value satisfy condition (ii). Let us denote the space spanned by these right-singular vectors with zero singular value (assume that there are p of them) $\{|\Psi_1\rangle,|\Psi_2\rangle,\ldots,|\Psi_p\rangle\}$ by $\mathbb{Z}_V$. The required sublattice scars are those which reside in $\mathbb{Z}_V$ and satisfy condition (i). We first construct the matrix $[\tilde{\mathbb{V}}_{n\times n}]_{ji}=(v_{ji}-\mathcal{N}\delta_{ji})$ and then take the projection to $\mathbb{Z}_V$: $[(\tilde{\mathbb{V}}_0)_{n\times p}]=[\tilde{\mathbb{V}}_{n\times n}]\times[\mathbb{M}_{n\times p}]$. The columns of $\mathbb{M}$ are formed by the column matrices $|\Psi_i\rangle$s. Again, the right-singular vectors of $\tilde{\mathbb{V}}_0$ with zero singular value will satisfy both conditions (i) and (ii). Using this method, we could only find solutions for $\mathcal{N}=\pm 2$ for the system sizes that we could numerically access.

We can decompose the sublattice scars into Fock states with equal (unequal) number of clockwise and anticlockwise flippable plaquettes on one sublattice. To do that, we simply divide the set $\{|f_i\rangle\}_n$ into the sets of equal and unequal clockwise and anticlockwise flippable plaquettes, $\{|f_i^{\rm eq}\rangle\}_{n_{\rm eq}}$ and $\{|f_i^{\rm uneq}\rangle\}_{n_{\rm uneq}}$. Then using the above method for the individual sets, we can find if any scar can be obtained from $\{|f_i^{\rm eq}\rangle\}_{n_{\rm eq}}$ and $\{|f_i^{\rm uneq}\rangle\}_{n_{\rm uneq}}$. At this point, it is worth stressing that the above method of obtaining sublattice scars is more efficient than the full ED, because in this method we use a small subspace of the full Hilbert space (see Table IV for a comparison).

We now address the construction of the set $\{|f_i\rangle\}_n$. For this, we need to start with certain "base states" that are Fock states that satisfy the sublattice constraint and repeatedly act $\mathcal{O}_{\rm kin}$ on those states to get other Fock states consistent with the sublattice constraint. Most of the subsequent states are produced from the base state where plaquettes are arranged in an alternate clockwise and anticlockwise flippable pattern on the active sublattice as shown in Fig. 7(a) for (4, 4) lattice and Fig. 7(f) for (6, 4) lattice. Note that it is enough to consider any one of the two Fock states related by $\mathbb{C}$ for this base state. First we put the base state in $\{|f_i\rangle\}_n$. When $\mathcal{O}_{\rm kin}$ acts on this base state, new Fock states are generated out of which only some are consistent with

TABLE IV. HSD and number of Fock states present in $\{|f_i^{\rm eq}\rangle\}_{n_{\rm eq}}$, $\{|F_i^{\rm eq}\rangle\}_{m_{\rm eq}}$, $\{|f_i^{\rm uneq}\rangle\}_{n_{\rm uneq}}$, and $\{|F_i^{\rm uneq}\rangle\}_{m_{\rm uneq}}$ for various lattices.

Lattice	HSD	$n_{\rm eq}$	$m_{\rm eq}$	$n_{\rm uneq}$	$m_{\rm uneq}$
6×4	32810	510	1392	552	1628
8×4	1159166	4662	16352	5984	20574
10×4	42240738	43896	186040	61720	248302
6×6	5482716	13778	55080	19260	72818

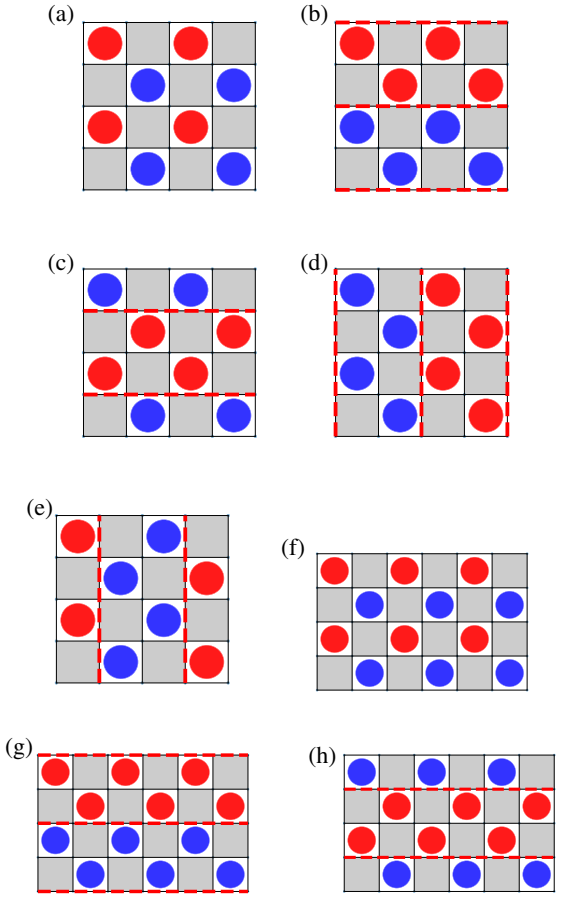

FIG. 7. Base states from which the set $\{|f_i\rangle\}_n$ can be obtained shown here. Panels (a) to (e) are for a (4, 4) lattice while panels (f) to (h) are for a (6, 4) lattice. Clockwise (anticlockwise) circulation of electric fluxes on a plaquette is shown by a red (blue) circle as in Fig. 1. The white (gray) plaquettes denote active (inactive) plaquettes with $\mathcal{O}_{\text{pot},\square} = 1(0)$ as in Fig. 4. Horizontal (vertical) partitions of width 2 are shown using dotted red lines as in Fig. 4.

the sublattice constraint, and we only insert these additional Fock states in $\{|f_i\rangle\}_n$. We then act $\mathcal{O}_{\text{kin}}$ on these newly added Fock states to generate more Fock states and consider only the states consistent with the sublattice constraint out of these newly generated states to insert in $\{|f_i\rangle\}_n$. At this stage, we avoid adding the Fock states which are already present in $\{|f_i\rangle\}_n$. We repeat this recursive process until there is no new Fock state to be added to the set $\{|f_i\rangle\}_n$. This procedure leaves out a few Fock states from the set $\{|f_i\rangle\}_n$. These "base states," which are consistent with the sublattice constraint, have the property that the action of $\mathcal{O}_{\text{kin}}$ on them produces no Fock state in the set $\{|f_i\rangle\}_n$ and, hence, these need to be inserted separately in $\{|f_i\rangle\}_n$. There is a simple rule to generate these extra base states to complete the set $\{|f_i\rangle\}_n$. We first divide the lattice into a close packing of parallel nonoverlapping horizontal or vertical partitions, each of width 2 and then arrange all the active plaquettes contained in a partition in a clockwise or anticlockwise manner. Once active plaquettes in a partition are arranged in a clockwise (anticlockwise) manner, its neighboring partitions must have active plaquettes with the opposite circulation. Lastly, the number of partitions with clockwise active plaquettes must equal that of partitions with anticlockwise active plaquettes in such a base state. Figures 7(b) to 7(e) show such base states for a (4, 4) lattice and Figs. 7(g) and 7(h) show such base states for the (6, 4) lattice. Note that only half of these base states are shown here with the other half easily generated by applying the charge conjugation operator $\mathbb{C}$.

V. PARENT HAMILTONIAN FOR SUBLATTICE SCARS

The sublattice scars discussed in the previous sections are midspectrum eigenstates of $\mathcal{H}_{\text{RK}}$ for any $\lambda \sim O(1)$. We can ask whether a parent Hamiltonian can be written for which these states are, in fact, ground states. One motivation for this is to substantiate the expectation, that although these scar states occur as high-energy excited states of a lattice Hamiltonian, they should not be dismissed as cutoff effects. On the contrary, as we show next, such states can also be realized in the low-energy physics of certain (gauge invariant) Hamiltonian, and therefore possibly survive the continuum limit. We do not however, have a rigorous proof of the latter and leave it for future investigation.

The following long-ranged Hamiltonian:

$$\begin{aligned}\mathcal{H}_{\text{LR}} &= \frac{1}{N_p}(\mathcal{O}_{\text{kin}})^2 + c\sum_{\square}(-1)^{\square}\mathcal{O}_{\text{pot},\square}, \\ &= \frac{1}{N_p}\sum_{\square_i,\square_j}(\mathcal{O}_{\text{kin},\square})_i(\mathcal{O}_{\text{kin},\square})_j \\ &\quad + c\sum_{\square}(-1)^{\square}\mathcal{O}_{\text{pot},\square}, \end{aligned} \tag{11}$$

which consists of an all-to-all two-plaquette interaction of the form $(\mathcal{O}_{\text{kin},\square})_i(\mathcal{O}_{\text{kin},\square})_j$, where the indices i and j run over all plaquettes, and another short-ranged staggered term involving $\mathcal{O}_{\text{pot},\square}$. The normalization of $1/N_p$ for the first term ensures that both the terms scale extensively with system size. Lastly, $c \neq 0$ is an arbitrary real parameter [which we choose to be O(1)].

For $c > 0$ ($c < 0$), all sublattice scars with $\mathcal{O}_{\text{kin}} = 0$ and active plaquettes on one (the other) sublattice become exact ground states of $\mathcal{H}_{\text{LR}}$ since both $(\mathcal{O}_{\text{kin}})^2$ and $c\sum_{\square}(-1)^{\square}\mathcal{O}_{\text{pot},\square}$ are minimized simultaneously. In fact, it is enough to focus on one particular sign of c. While sublattice scars with active plaquettes on one sublattice become ground states with energy $E_0 = -|c|\frac{N_p}{2}$, the other set of sublattice scars (where the active plaquettes reside on the other sublattice) become exact eigenstates of $\mathcal{H}_{\text{LR}}$ with energy $-E_0 = |c|\frac{N_p}{2}$. The sublattice scars with $\mathcal{O}_{\text{kin}} = \pm 2$

become degenerate eigenstates of $\mathcal{H}_{\rm LR}$ with energies $E_{s,\mp} = (\frac{4}{N_p}) \mp |c| \frac{N_p}{2}$, depending on which sublattice the active plaquettes belong to.

The triangle relation [Eq. (10)] connecting sublattice scars with $\mathcal{O}_{\rm kin} = \pm 2$ with particular sublattices scars with $\mathcal{O}_{\rm kin} = 0$ has a nice interpretation in terms of the states of $\mathcal{H}_{\rm LR}$. The sublattice scar $|\psi_{s,0}\rangle$, composed of Fock states with unequal number of clockwise and anticlockwise flippable active plaquettes, is a ground state of $\mathcal{H}_{\rm LR}$ (with an appropriate sign of c to choose the sublattice). The state $|\psi_{s,+2}\rangle - \mathcal{C}_\alpha |\psi_{s,+2}\rangle$ is an eigenstate of $\mathcal{H}_{\rm LR}$ with energy $E_{s,-} = (\frac{4}{N_p}) - |c| \frac{N_p}{2}$. Note that $|\psi_{s,+2}\rangle$ and $\mathcal{C}_\alpha |\psi_{s,+2}\rangle$ have different energies with respect to $\mathcal{H}_{\rm RK}$, so their difference is not an eigenstate of $\mathcal{H}_{\rm RK}$. Since the operator $\mathcal{O}$ leads to a sign change (no sign change) for Fock states with $(\frac{N_p}{4}+1, \frac{N_p}{4}-1)$ $[(\frac{N_p}{4}-1, \frac{N_p}{4}+1)]$ clockwise and anticlockwise active plaquettes, it is clear that $\mathcal{O}^2 = 1$. Using this, we can rewrite Eq. (10) as

$$(|\psi_{s,+2}\rangle - \mathcal{C}_\alpha |\psi_{s,+2}\rangle) \propto \mathcal{O} |\psi_{s,0}\rangle, \tag{12}$$

where $\mathcal{O}$ can now be interpreted to creates a finite-energy excitation, with an energy of $\Delta E = \frac{4}{N_p}$, when acting on a ground state of $\mathcal{H}_{\rm LR}$. However, given the form of $\mathcal{O}$, it does not seem possible to write it as a sum of local (in space) operators.

We have verified numerically using ED on finite (L_x, L_y) lattice that the ground states (with energy $-E_0$), excited states with energy $+E_0$, and energies $E_{s,\mp}$ are all sublattice scars. ED also reveals a rich structure in the spectrum of $\mathcal{H}_{\rm LR}$. We display the data for a system with dimension (12, 2) with $c = 1$ in Fig. 8. Figure 8(a) shows Shannon entropy for each eigenstate $|\Psi\rangle$ which can be calculated using $-\sum_\alpha |\Psi_\alpha|^2 \ln |\Psi_\alpha|^2$, where $|\Psi\rangle = \sum_\alpha \Psi_\alpha |\alpha\rangle$ when the eigenstate is expressed in the computational basis $|\alpha\rangle$. The Shannon entropy shows several prominent dips as a function of energy E indicating the presence of several eigenstates which are much more localized in the Hilbert space compared to neighboring eigenstates. Interestingly, the density of states, $\rho(E)$, extracted from the eigenvalues of $\mathcal{H}_{\rm LR}$ display a rather intricate structure as well with several local maxima [Fig. 8(b)]. The positions of these local maxima in $\rho(E)$ seem to be strongly correlated to the appearance of anomalous dips in the Shannon entropy.

Finally, from ED on finite lattices, the zero energy states of $\mathcal{H}_{\rm LR}$ stay unchanged (apart from mixing with each other) as a function of c. This implies that these must be simultaneous eigenstates of $\mathcal{O}_{\rm kin}$ and $c \sum_\square (-1)^\square \mathcal{O}_{{\rm pot},\square}$. We will discuss these anomalous zero modes, which are distinct from the sublattice scars, in the next section.

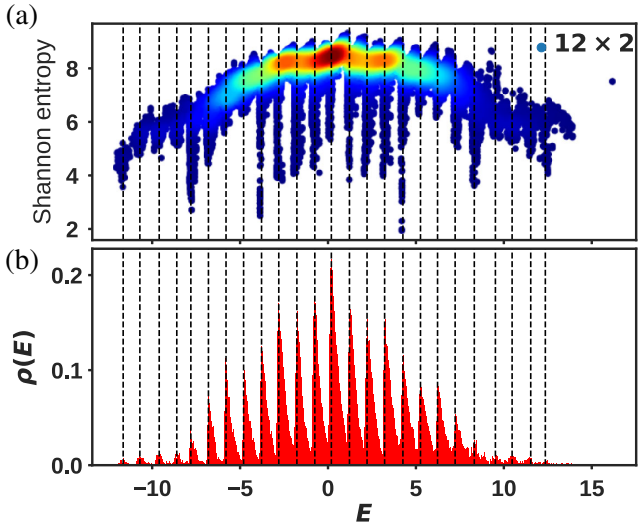

FIG. 8. (a) Behavior of the Shannon entropy shown for all the eigenstates of $\mathcal{H}_{\rm LR}$ for a system of size (12, 2). (b) Density of states, $\rho(E)$, plotted as a function of energy for the same system. Both calculations use $c = 1.0$. In (b), 512 bins have been taken to find density of states. Vertical dotted lines are plotted at the positions of local maxima of DOS by visual inspection. In (a), the density of states is indicated by a color map where warmer color corresponds to higher density of states.

VI. MORE QUANTUM SCARS FROM ZERO MODES

We now discuss a different variety of quantum many-body scars that are again composed of the null space of $\mathcal{O}_{\rm kin}$ but have different properties from the sublattice scars. While the sublattice scars are simultaneous eigenstates of the noncommuting operators $\mathcal{O}_{\rm kin}$ and $\sum_\square \mathcal{O}_{{\rm pot},\square}$, these scars are instead simultaneous zero modes of $\mathcal{O}_{\rm kin}$ and $\sum_\square (-1)^\square \mathcal{O}_{{\rm pot},\square}$. These anomalous states are thus exact zero modes of $\mathcal{H}_{\rm st}$ that stay unchanged as a function of λ. We refer the reader to Ref. [83] for a similar scarring mechanism in a spin chain. As discussed in a previous section, $\mathcal{H}_{\rm st}$ satisfies an index theorem at any value of λ and, hence, its spectrum has an E to $-E$ symmetry as well as exponentially many (in system size) zero modes (see Table I and Fig. 2). However, since $\mathcal{O}_{\rm kin}$ and $\sum_\square (-1)^\square \mathcal{O}_{{\rm pot},\square}$ do not commute with each other, these zero modes, apart from the ones that are simultaneous eigenstates of both the terms, keep changing in a nontrivial fashion. In fact, any typical zero mode of $\mathcal{H}_{\rm st}$ is expected to satisfy ETH and locally mimic a featureless infinite temperature state. However, the zero modes that stay unchanged with λ are expected to violate the ETH [68,83].

The anomalous nature of these simultaneous zero modes can be clearly demonstrated by calculating the Shannon entropy of all the eigenstates of $\mathcal{H}_{\rm st}$ [Eq. (3)] for $\lambda \sim O(1)$ using ED on finite lattices. Figure 9 displays the data for (12, 2) at $\lambda = 1.1$ and for (6, 4) at $\lambda = 1.0$. It is clear from

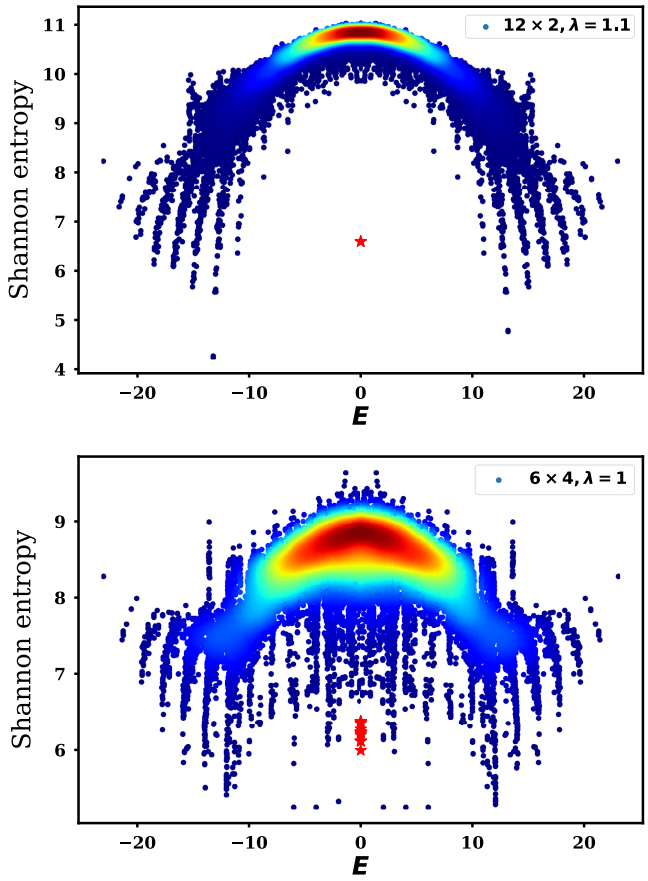

FIG. 9. Shannon entropy for all the eigenstates of $\mathcal{H}_{\rm st}$ [Eq. (3)] plotted as a function of energy E with panel (a) showing data for system of size (12, 2) and panel (b) showing data for (6,4). In both plots, the simultaneous zero modes of $\mathcal{O}_{\rm kin}$ and $\sum_{\square}(-1)^{\square}\mathcal{O}_{{\rm pot},\square}$ are shown using a different font and color (red stars). The density of states is indicated by the same color map in both panels where warmer color corresponds to higher density of states.

both panels that the simultaneous zero modes have anomalously low Shannon entropy compared to the typical values for neighboring eigenstates, demonstrating that these states do violate the ETH. From both plots, it is also clear that there may be other anomalous high-energy states in the spectrum of $\mathcal{H}_{\rm st}$ but we only focus on the ETH-violating zero modes here.

TABLE V. Scaling of the number of anomalous zero modes of $\mathcal{H}_{\rm st}$ as a function of system size extracted from ED.

Lattice	Anomalous zero modes of $\mathcal{H}_{\rm st}$
$L_x \times 2$	2
4×4	8
6×4	14

The number of these simultaneous zero modes is given in Table V. Just like in the case of sublattice scars, their number stays fixed with L_x in the thin torus limit of $L_y = 2$, while it increases with L_x for wider ladders. These quantum scars are eigenstates of the charge conjugation, $\mathbb{C}$, with half of them possessing $\mathbb{C} = +1$ ($\mathbb{C} = -1$). For $(L_x, 2)$ systems, the unique scar with $\mathbb{C} = 1$ ($\mathbb{C} = -1$) is also a momentum eigenstate with $(k_x, k_y) = (0, 0)$ $(= (\pi, \pi))$ with respect to translations by one lattice unit in both directions.

While we do not yet have an analytic understanding of these quantum scars, we show the form of these states in the thin torus limit of $L_y = 2$ for $L_x = 8$. The representative Fock states (denoted as $|f_i\rangle$ where i ranges from 1 to 6) that contribute to create the two simultaneous zero modes for a (8, 2) lattice are shown in Fig. 10. Given any of the representative states, $|f_i\rangle$, one can build a basis state $|f_i(k_x, k_y)\rangle = \frac{1}{\sqrt{N_i}} \sum_{x=1}^{L_x} \sum_{y=1}^{L_y} e^{-i(k_x x + k_y y)} T_Y^y T_X^x |f_i\rangle$ that carries a well-defined momentum (k_x, k_y) with respect to translations by one lattice unit in (x, y) implemented by the operators (T_X, T_Y). Note that the renormalization N_i represents the number of distinct Fock states that can be obtained from $|f_i\rangle$ by translations and equals $N_i = 6$ for $i = 1$ to 5 and $N_6 = 2$. The two anomalous zero modes

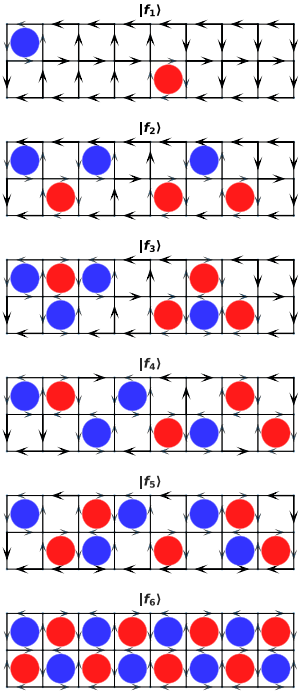

FIG. 10. The representative states ($|f_i\rangle$) that build the two anomalous zero modes of $\mathcal{H}_{\rm st}$ for a system of dimension (8, 2). The electric fluxes are shown for each link of each of the representative states by arrows. Clockwise (anticlockwise) circulation of electric fluxes on a plaquette is shown by a red (blue) circle as in Fig. 1.

of $\mathcal{H}_{\rm st}$ for (8, 2) can now be compactly written as follows:

$$|\Psi_{s,+1}\rangle = \frac{1}{\sqrt{41}}[\sqrt{3}|f_1(0,0)\rangle] + \sqrt{3}|f_2(0,0)\rangle - \sqrt{3}|f_3(0,0)\rangle - \sqrt{3}|f_4(0,0)\rangle + \sqrt{3}|f_5(0,0)\rangle + |f_6(0,0)\rangle],$$
$$|\Psi_{s,-1}\rangle = \frac{1}{\sqrt{41}}[\sqrt{3}|f_1(\pi,\pi)\rangle] - \sqrt{3}|f_2(\pi,\pi)\rangle + \sqrt{3}|f_3(\pi,\pi)\rangle - \sqrt{3}|f_4(\pi,\pi)\rangle - \sqrt{3}|f_5(\pi,\pi)\rangle - |f_6(\pi,\pi)\rangle], \quad (13)$$

where $|\Psi_{s,+1}\rangle$ carries momentum $(k_x, k_y) = (0, 0)$ and $\mathbb{C} = +1$ while $|\Psi_{s,-1}\rangle$ has $(k_x, k_y) = (\pi, \pi)$ and $\mathbb{C} = -1$. From the structure of the representative Fock states in Fig. 10, it is also clear that these states do not have a sublattice structure of active and inactive plaquettes in real space.

VII. CONCLUSION AND OUTLOOK

In conclusion, we have considered two $U(1)$ quantum link gauge theory Hamiltonians in their spin-$\frac{1}{2}$ representation on (L_x, L_y) square lattices with periodic boundary conditions in both directions and even L_x, L_y. We specifically target the largest superselection sector with zero charge at each site and zero winding numbers in both directions. Both the link models are composed of plaquette operators, $\mathcal{O}_{\rm kin,\square}$ and $\mathcal{O}_{\rm pot,\square}$, defined on elementary plaquettes of the lattice where $\mathcal{O}_{\rm kin,\square}$ changes a clockwise circulation of electric fluxes on a plaquette to anticlockwise and vice versa while $\mathcal{O}_{\rm pot,\square}$ acts as a counting operator for such a plaquette. While the first Hamiltonian that we consider, $\mathcal{H}_{\rm RK} = -\sum_{\square} \mathcal{O}_{\rm kin,\square} + \lambda \sum_{\square} \mathcal{O}_{\rm pot,\square}$ [Eq. (2)], is a standard Rokhsar-Kivelson model, the second Hamiltonian, $\mathcal{H}_{\rm st} = -\sum_{\square} \mathcal{O}_{\rm kin,\square} + \lambda \sum_{\square} (-1)^{\square} \mathcal{O}_{\rm pot,\square}$ [Eq. (3)] has a staggered potential term that depends on the sublattice location of the plaquette. Both models represent nonintegrable Abelian lattice gauge theories without dynamical matter. Both theories become identical when $\lambda = 0$ where the Hamiltonian, which can be represented as $\mathcal{O}_{\rm kin} = -\sum_{\square} \mathcal{O}_{\rm kin,\square}$, only consists of off-diagonal terms in the electric flux basis. In this limit, the system supports an exponentially large number (in system size) of exact midspectrum zero modes that are protected by an index theorem. The index theorem is immediately lifted when $\lambda \neq 0$ for $\mathcal{H}_{\rm RK}$ while it stays preserved for any λ for $\mathcal{H}_{\rm st}$. The zero modes of $\mathcal{O}_{\rm kin}$ as well as $\mathcal{H}_{\rm st}$ are expected to locally mimic a featureless infinite temperature thermal state from the eigenstate thermalization hypothesis.

We show the existence of several anomalous high-energy eigenstates, that violate the eigenstate thermalization hypothesis, in both these quantum link gauge theory Hamiltonians. We dub one class of these anomalous states as sublattice scars. These sublattice scars, $|\psi_s\rangle$, are highly structured in terms of $\mathcal{O}_{\rm pot,\square}$ with $\mathcal{O}_{\rm pot,\square}|\psi_s\rangle = |\psi_s\rangle$ for all elementary plaquettes on one sublattice and $\mathcal{O}_{\rm pot,\square}|\psi_s\rangle = 0$ on the elementary plaquettes that belong to the other sublattice. Furthermore, these states are eigenstates of $\mathcal{O}_{\rm kin}$, with eigenvalues 0 or ± 2. A class of sublattice scars with $\mathcal{O}_{\rm kin} = 0$ have a simple representation in terms of coverings of emergent dimers (singlets) and their number scales as $O(2^{L_x/2+1} + 2^{L_y/2+1} - 4)$ for $L_x, L_y \gg 1$, thus showing their presence even in two dimensions. These short singlet scars explain all sublattice scars that occur in the thin-torus limit of $L_y = 2$ and L_x arbitrary. However, wider systems with $L_y \geq 4$ have several sublattice scars that are beyond this description in terms of singlets. We also find sublattice scars with $\mathcal{O}_{\rm kin} = \pm 2$ for $L_y \geq 4$ and demonstrate a nontrivial "triangle relation" between sublattice scars with $\mathcal{O}_{\rm kin} = +2$, $\mathcal{O}_{\rm kin} = -2$, and $\mathcal{O}_{\rm kin} = 0$. The analysis of the structure of the nonsinglet scars was greatly aided by a numerical approach which directly focused on the relevant state space for these high-energy states, instead of usual exact diagonalization techniques which require the full Hilbert space to construct high-energy eigenstates. We further discuss a long-ranged parent Hamiltonian, $\mathcal{H}_{\rm LR}$ [Eq. (11)], which gives all sublattice scars with $\mathcal{O}_{\rm kin} = 0$ as unique ground states and sublattice scars with $\mathcal{O}_{\rm kin} = \pm 2$ as finite energy excitations. The triangle relation can be interpreted as a quasiparticle operator acting on certain ground states of this long-ranged Hamiltonian to give finite energy excitations. Apart from these sublattice scars, we find additional anomalous zero modes of $\mathcal{O}_{\rm kin}$ that are also exact zero modes of $(-1)^{\square}\mathcal{O}_{\rm pot,\square}$, and hence anomalous zero modes of $\mathcal{H}_{\rm st}$ that do not change with coupling λ.

The results presented here immediately suggest several future avenues of study. One of the conceptually challenging questions is to establish the presence of such anomalous eigenstates in the limit when the lattice discretization is removed, i.e., directly in the continuum field theory. One way we have tried to motivate that this indeed might be the case is to construct a different Hamiltonian, where such states occur in the ground state manifold, indicating that the scarring phenomena resulting in the eigenstates reported here can exist beyond a single Hamiltonian and energy window. However, a detailed analysis is required. It might be interesting to attempt the description of these quantum scars using the language of path integrals, using which it might be easier to establish their behavior in the continuum limit.

It might also be worthwhile to explore if addition of local kinetic energy terms can also give rise to the singlet scar states as ground states. Moreover, the spectrum of $\mathcal{H}_{\rm st}$ seems to suggest the presence of several other anomalous high-energy states apart from the ones discussed here. We leave this as an interesting question for future studies. A deeper understanding of both the anomalous zero modes of $\mathcal{H}_{\rm st}$ and the nonsinglet sublattice scars would be highly desirable. Additionally, the ground state physics, and possible phase transitions of both the $\mathcal{H}_{\rm LR}$ and the $\mathcal{H}_{\rm st}$ would be an exciting line of future research, given the

recent interest of realizing lattice gauge theories on quantum simulator platforms. Finally, another interesting question is to search for similar scars in spin-S, with $S \geq 1$, quantum link gauge theories without dynamical matter fields as well as in non-Abelian versions.

ACKNOWLEDGMENTS

We would like to acknowledge the computational resources provided by IACS and SINP. D. B. acknowledges assistance from SERB Starting Grant No. SRG/2021/000396-C from the DST (Government of India). P. S. acknowledges support from ERC AdG NOQIA; MCIN/AEI [Grants No. PGC2018-0910.13039/501100011033, No. CEX2019-000910-S/10.13039/501100011033, Plan National FIDEUA PID2019–106901 GB-I00, Plan National STAMEENA PID2022-139099NB-I00 project funded by MCIN/AEI/10.13039/501100011033 and by the "European Union NextGenerationEU/PRTR" (PRTR-C17.I1), Formación de Personal Investigador (FPI); QUANTERA MAQS PCI2019-111828-2]; QUANTERA DYNAMITE PCI2022-132919 (QuantERA II Programme cofunded by European Union's Horizon 2020 program under Grant Agreement No. 101017733), Ministry of Economic Affairs and Digital Transformation of the Spanish Government through the QUANTUM ENIA project call—Quantum Spain project, and by the European Union through the Recovery, Transformation, and Resilience Plan—NextGenerationEU within the framework of the Digital Spain 2026 Agenda; Fundació Cellex; Fundació Mir-Puig; Generalitat de Catalunya (European Social Fund FEDER and CERCA program, AGAUR Grant No. 2021 SGR 01452, QuantumCAT U16-011424, cofunded by ERDF Operational Program of Catalonia 2014-2020); Barcelona Supercomputing Center MareNostrum (Grant No. FI-2023-1-0013); EU Quantum Flagship (Grants No. PASQuanS2.1, No. 101113690); EU Horizon 2020 FET-OPEN OPTOlogic (Grant No. 899794); EU Horizon Europe Program (Grant Agreement No. 101080086—NeQST), ICFO Internal "QuantumGaudi" project; European Union's Horizon 2020 program under the Marie Sklodowska-Curie Grant Agreement No. 847648; "La Caixa" Junior Leaders fellowships, La Caixa" Foundation (ID 100010434): Grant No. CF/BQ/PR23/11980043. Views and opinions expressed are, however, those of the author(s) only and do not necessarily reflect those of the European Union, European Commission, European Climate, Infrastructure and Environment Executive Agency (CINEA), or any other granting authority. Neither the European Union nor any granting authority can be held responsible for them.

[1] R. L. Workman *et al.* (Particle Data Group), Review of particle physics, Prog. Theor. Exp. Phys. **2022**, 083C01 (2022).
[2] G. S. Ramos and M. V. T. Machado, Investigating entanglement entropy at small-x in DIS off protons and nuclei, Phys. Rev. D **101**, 074040 (2020).
[3] M. Fabbrichesi, R. Floreanini, and G. Panizzo, Testing Bell inequalities at the LHC with top-quark pairs, Phys. Rev. Lett. **127**, 161801 (2021).
[4] John Preskill, Quantum computing in the NISQ era and beyond, Quantum **2**, 79 (2018).
[5] Francesco Tacchino, Alessandro Chiesa, Stefano Carretta, and Dario Gerace, Quantum computers as universal quantum simulators: State-of-the-art and perspectives, Adv. Quantum Technol. **3**, 1900052 (2019).
[6] Roland C. Farrell, Marc Illa, Anthony N. Ciavarella, and Martin J. Savage, Scalable circuits for preparing ground states on digital quantum computers: The Schwinger model vacuum on 100 qubits, arXiv:2308.04481.
[7] Ron Belyansky, Seth Whitsitt, Niklas Mueller, Ali Fahimniya, Elizabeth R. Bennewitz, Zohreh Davoudi, and Alexey V. Gorshkov, High-energy collision of quarks and hadrons in the Schwinger model: From tensor networks to circuit QED, arXiv:2307.02522.
[8] M. C. Bañuls *et al.*, Simulating lattice gauge theories within quantum technologies, Eur. Phys. J. D **74**, 165 (2020).
[9] Christian W. Bauer, Zohreh Davoudi, Natalie Klco, and Martin J. Savage, Quantum simulation of fundamental particles and forces, Nat. Rev. Phys. **5**, 420 (2023).
[10] Kenneth Heitritter, Yannick Meurice, and Stephen Mrenna, Prolegomena to a hybrid Classical/Rydberg simulator for hadronization (QuPYTH), arXiv:2212.02476.
[11] D. Banerjee, S. Caspar, F. J. Jiang, J. H. Peng, and U. J. Wiese, Nematic confined phases in the U(1) quantum link model on a triangular lattice: Near-term quantum computations of string dynamics on a chip, Phys. Rev. Res. **4**, 023176 (2022).
[12] Jad C. Halimeh and Philipp Hauke, Stabilizing gauge theories in quantum simulators: A brief review, arXiv:2204.13709.
[13] Yasar Y. Atas, Jan F. Haase, Jinglei Zhang, Victor Wei, Sieglinde M. L. Pfaendler, Randy Lewis, and Christine A. Muschik, Simulating one-dimensional quantum chromodynamics on a quantum computer: Real-time evolutions of tetra- and pentaquarks, Phys. Rev. Res. **5**, 033184 (2023).
[14] Alberto Di Meglio *et al.*, Quantum computing for high-energy physics: State of the art and challenges. Summary of the QC4HEP Working Group, arXiv:2307.03236.
[15] E. A. Martinez *et al.*, Real-time dynamics of lattice gauge theories with a few-qubit quantum computer, Nature (London) **534**, 516 (2016).
[16] Alexander Mil, Torsten V. Zache, Apoorva Hegde, Andy Xia, Rohit P. Bhatt, Markus K. Oberthaler, Philipp Hauke,

Jürgen Berges, and Fred Jendrzejewski, A scalable realization of local U(1) gauge invariance in cold atomic mixtures, Science **367**, 1128 (2020).
[17] Bing Yang, Hui Sun, Robert Ott, Han-Yi Wang, Torsten V. Zache, Jad C. Halimeh, Zhen-Sheng Yuan, Philipp Hauke, and Jian-Wei Pan, Observation of gauge invariance in a 71-site Bose–Hubbard quantum simulator, Nature (London) **587**, 392 (2020).
[18] N. Klco, E. F. Dumitrescu, A. J. McCaskey, T. D. Morris, R. C. Pooser, M. Sanz, E. Solano, P. Lougovski, and M. J. Savage, Quantum-classical computation of Schwinger model dynamics using quantum computers, Phys. Rev. A **98**, 032331 (2018).
[19] J. M. Deutsch, Quantum statistical mechanics in a closed system, Phys. Rev. A **43**, 2046 (1991).
[20] Mark Srednicki, Chaos and quantum thermalization, Phys. Rev. E **50**, 888 (1994).
[21] Marcos Rigol, Vanja Dunjko, and Maxim Olshanii, Thermalization and its mechanism for generic isolated quantum systems, Nature (London) **452**, 854 (2008).
[22] C. J. Turner, A. A. Michailidis, D. A. Abanin, M. Serbyn, and Z. Papić, Weak ergodicity breaking from quantum many-body scars, Nat. Phys. **14**, 745 (2018).
[23] C. J. Turner, A. A. Michailidis, D. A. Abanin, M. Serbyn, and Z. Papić, Quantum scarred eigenstates in a rydberg atom chain: Entanglement, breakdown of thermalization, and stability to perturbations, Phys. Rev. B **98**, 155134 (2018).
[24] M. Schulz, C. A. Hooley, R. Moessner, and F. Pollmann, Stark many-body localization, Phys. Rev. Lett. **122**, 040606 (2019).
[25] Pablo Sala, Tibor Rakovszky, Ruben Verresen, Michael Knap, and Frank Pollmann, Ergodicity breaking arising from Hilbert space fragmentation in dipole-conserving Hamiltonians, Phys. Rev. X **10**, 011047 (2020).
[26] Vedika Khemani, Michael Hermele, and Rahul Nandkishore, Localization from Hilbert space shattering: From theory to physical realizations, Phys. Rev. B **101**, 174204 (2020).
[27] Hannes Bernien, Sylvain Schwartz, Alexander Keesling, Harry Levine, Ahmed Omran, Hannes Pichler, Soonwon Choi, Alexander S. Zibrov, Manuel Endres, Markus Greiner, Vladan Vuletić, and Mikhail D. Lukin, Probing many-body dynamics on a 51-atom quantum simulator, Nature (London) **551**, 579 (2017).
[28] W. Morong, F. Liu, P. Becker, K. S. Collins, L. Feng, A. Kyprianidis, G. Pagano, T. You, A. V. Gorshkov, and C. Monroe, Observation of stark many-body localization without disorder, Nature (London) **599**, 393 (2021).
[29] Oskar Vafek, Nicolas Regnault, and B. Andrei Bernevig, Entanglement of exact excited eigenstates of the Hubbard model in arbitrary dimension, SciPost Phys. **3**, 043 (2017).
[30] Soonwon Choi, Christopher J. Turner, Hannes Pichler, Wen Wei Ho, Alexios A. Michailidis, Zlatko Papić, Maksym Serbyn, Mikhail D. Lukin, and Dmitry A. Abanin, Emergent SU(2) dynamics and perfect quantum many-body scars, Phys. Rev. Lett. **122**, 220603 (2019).
[31] Wen Wei Ho, Soonwon Choi, Hannes Pichler, and Mikhail D. Lukin, Periodic orbits, entanglement, and quantum many-body scars in constrained models: Matrix product state approach, Phys. Rev. Lett. **122**, 040603 (2019).
[32] Cheng-Ju Lin and Olexei I. Motrunich, Exact quantum many-body scar states in the rydberg-blockaded atom chain, Phys. Rev. Lett. **122**, 173401 (2019).
[33] Thomas Iadecola, Michael Schecter, and Shenglong Xu, Quantum many-body scars from magnon condensation, Phys. Rev. B **100**, 184312 (2019).
[34] Naoto Shiraishi, Connection between quantum-many-body scars and the Affleck–Kennedy–Lieb–Tasaki model from the viewpoint of embedded Hamiltonians, J. Stat. Mech. (2019) 083103.
[35] Sanjay Moudgalya, Nicolas Regnault, and B. Andrei Bernevig, Entanglement of exact excited states of Affleck-Kennedy-Lieb-Tasaki models: Exact results, many-body scars, and violation of the strong eigenstate thermalization hypothesis, Phys. Rev. B **98**, 235156 (2018).
[36] Sanjay Moudgalya, Stephan Rachel, B. Andrei Bernevig, and Nicolas Regnault, Exact excited states of nonintegrable models, Phys. Rev. B **98**, 235155 (2018).
[37] K. Pakrouski, P. N. Pallegar, F. K. Popov, and I. R. Klebanov, Many-body scars as a group invariant sector of Hilbert space, Phys. Rev. Lett. **125**, 230602 (2020).
[38] Daniel K. Mark, Cheng-Ju Lin, and Olexei I. Motrunich, Unified structure for exact towers of scar states in the Affleck-Kennedy-Lieb-Tasaki and other models, Phys. Rev. B **101**, 195131 (2020).
[39] Naoyuki Shibata, Nobuyuki Yoshioka, and Hosho Katsura, Onsager's scars in disordered spin chains, Phys. Rev. Lett. **124**, 180604 (2020).
[40] Sudip Sinha and S. Sinha, Chaos and quantum scars in Bose-Josephson junction coupled to a bosonic mode, Phys. Rev. Lett. **125**, 134101 (2020).
[41] Hongzheng Zhao, Joseph Vovrosh, Florian Mintert, and Johannes Knolle, Quantum many-body scars in optical lattices, Phys. Rev. Lett. **124**, 160604 (2020).
[42] K. Pakrouski, P. N. Pallegar, F. K. Popov, and I. R. Klebanov, Group theoretic approach to many-body scar states in fermionic lattice models, Phys. Rev. Res. **3**, 043156 (2021).
[43] Bhaskar Mukherjee, Sourav Nandy, Arnab Sen, Diptiman Sen, and K. Sengupta, Collapse and revival of quantum many-body scars via floquet engineering, Phys. Rev. B **101**, 245107 (2020).
[44] Bhaskar Mukherjee, Arnab Sen, Diptiman Sen, and K. Sengupta, Dynamics of the vacuum state in a periodically driven rydberg chain, Phys. Rev. B **102**, 075123 (2020).
[45] Bhaskar Mukherjee, Arnab Sen, Diptiman Sen, and K. Sengupta, Restoring coherence via aperiodic drives in a many-body quantum system, Phys. Rev. B **102**, 014301 (2020).
[46] Frank Schindler, Nicolas Regnault, and B. Andrei Bernevig, Exact quantum scars in the chiral non-linear Luttinger liquid, Phys. Rev. B **105**, 035146 (2022).
[47] Bhaskar Mukherjee, Arnab Sen, and K. Sengupta, Periodically driven rydberg chains with staggered detuning, Phys. Rev. B **106**, 064305 (2022).
[48] Bhaskar Mukherjee, Zi Cai, and W. Vincent Liu, Constraint-induced breaking and restoration of ergodicity in spin-1 pxp models, Phys. Rev. Res. **3**, 033201 (2021).
[49] Paul A. McClarty, Masudul Haque, Arnab Sen, and Johannes Richter, Disorder-free localization and many-body

quantum scars from magnetic frustration, Phys. Rev. B **102**, 224303 (2020).
[50] Volker Karle, Maksym Serbyn, and Alexios A. Michailidis, Area-law entangled eigenstates from nullspaces of local Hamiltonians, Phys. Rev. Lett. **127**, 060602 (2021).
[51] Bhaskar Mukherjee, Debasish Banerjee, K. Sengupta, and Arnab Sen, Minimal model for Hilbert space fragmentation with local constraints, Phys. Rev. B **104**, 155117 (2021).
[52] Anwesha Chattopadhyay, Bhaskar Mukherjee, Krishnendu Sengupta, and Arnab Sen, Strong Hilbert space fragmentation via emergent quantum drums in two dimensions, SciPost Phys. **14**, 146 (2023).
[53] Sanjay Moudgalya, B. Andrei Bernevig, and Nicolas Regnault, Quantum many-body scars and Hilbert space fragmentation: A review of exact results, Rep. Prog. Phys. **85**, 086501 (2022).
[54] Shailesh Chandrasekharan and U.-J. Wiese, Quantum link models: A discrete approach to gauge theories, Nucl. Phys. **B492**, 455 (1997).
[55] D. Banerjee, F.-J. Jiang, P. Widmer, and U.-J. Wiese, The $(2+1)$-d u(1) quantum link model masquerading as deconfined criticality, J. Stat. Mech. (2013) P12010.
[56] Uwe-Jens Wiese, Towards quantum simulating QCD, Nucl. Phys. **A931**, 246 (2014).
[57] Michael Hermele, Matthew P. A. Fisher, and Leon Balents, Pyrochlore photons: Theu(1)spin liquid in as=12three-dimensional frustrated magnet, Phys. Rev. B **69**, 064404 (2004).
[58] Daniel S. Rokhsar and Steven A. Kivelson, Superconductivity and the quantum hard-core dimer gas, Phys. Rev. Lett. **61**, 2376 (1988).
[59] Federica M. Surace, Paolo P. Mazza, Giuliano Giudici, Alessio Lerose, Andrea Gambassi, and Marcello Dalmonte, Lattice gauge theories and string dynamics in rydberg atom quantum simulators, Phys. Rev. X **10**, 021041 (2020).
[60] D. Banerjee, M. Dalmonte, M. Muller, E. Rico, P. Stebler, U. J. Wiese, and P. Zoller, Atomic quantum simulation of dynamical gauge fields coupled to fermionic matter: From string breaking to evolution after a quench, Phys. Rev. Lett. **109**, 175302 (2012).
[61] Subir Sachdev, K. Sengupta, and S. M. Girvin, Mott insulators in strong electric fields, Phys. Rev. B **66**, 075128 (2002).
[62] Igor Lesanovsky and Hosho Katsura, Interacting fibonacci anyons in a rydberg gas, Phys. Rev. A **86**, 041601 (2012).
[63] Jean-Yves Desaules, Debasish Banerjee, Ana Hudomal, Zlatko Papić, Arnab Sen, and Jad C. Halimeh, Weak ergodicity breaking in the Schwinger model, Phys. Rev. B **107**, L201105 (2023).
[64] Jean-Yves Desaules, Ana Hudomal, Debasish Banerjee, Arnab Sen, Zlatko Papić, and Jad C. Halimeh, Prominent quantum many-body scars in a truncated Schwinger model, Phys. Rev. B **107**, 205112 (2023).
[65] Adith Sai Aramthottil, Utso Bhattacharya, Daniel González-Cuadra, Maciej Lewenstein, Luca Barbiero, and Jakub Zakrzewski, Scar states in deconfined $\mathbb{z}_2$ lattice gauge theories, Phys. Rev. B **106**, L041101 (2022).
[66] Tomoya Hayata and Yoshimasa Hidaka, String-net formulation of Hamiltonian lattice Yang-Mills theories and quantum many-body scars in a nonAbelian gauge theory, J. High Energy Phys. 09 (2023) 126.
[67] Zhihao Lan and Stephen Powell, Eigenstate thermalization hypothesis in quantum dimer models, Phys. Rev. B **96**, 115140 (2017).
[68] Debasish Banerjee and Arnab Sen, Quantum scars from zero modes in an Abelian lattice gauge theory on ladders, Phys. Rev. Lett. **126**, 220601 (2021).
[69] Saptarshi Biswas, Debasish Banerjee, and Arnab Sen, Scars from protected zero modes and beyond in $U(1)$ quantum link and quantum dimer models, SciPost Phys. **12**, 148 (2022).
[70] R. Moessner, S. L. Sondhi, and Eduardo Fradkin, Short-ranged resonating valence bond physics, quantum dimer models, and ising gauge theories, Phys. Rev. B **65**, 024504 (2001).
[71] Nic Shannon, Grégoire Misguich, and Karlo Penc, Cyclic exchange, isolated states, and spinon deconfinement in an xxz Heisenberg model on the checkerboard lattice, Phys. Rev. B **69**, 220403 (2004).
[72] Nic Shannon, Olga Sikora, Frank Pollmann, Karlo Penc, and Peter Fulde, Quantum ice: A quantum Monte Carlo study, Phys. Rev. Lett. **108**, 067204 (2012).
[73] D. Banerjee, M. Bögli, C. P. Hofmann, F. J. Jiang, P. Widmer, and U. J. Wiese, Interfaces, strings, and a soft mode in the square lattice quantum dimer model, Phys. Rev. B **90**, 245143 (2014).
[74] D. Banerjee, M. Bögli, C. P. Hofmann, F. J. Jiang, P. Widmer, and U. J. Wiese, Finite-volume energy spectrum, fractionalized strings, and low-energy effective field theory for the quantum dimer model on the square lattice, Phys. Rev. B **94**, 115120 (2016).
[75] Tom Oakes, Stephen Powell, Claudio Castelnovo, Austen Lamacraft, and Juan P. Garrahan, Phases of quantum dimers from ensembles of classical stochastic trajectories, Phys. Rev. B **98**, 064302 (2018).
[76] Xiaoxue Ran, Zheng Yan, Yan-Cheng Wang, Junchen Rong, Yang Qi, and Zi Yang Meng, Fully packed quantum loop model on the square lattice: Phase diagram and application for rydberg atoms, Phys. Rev. B **107**, 125134 (2023).
[77] Michael Schecter and Thomas Iadecola, Many-body spectral reflection symmetry and protected infinite-temperature degeneracy, Phys. Rev. B **98**, 035139 (2018).
[78] John Kogut and Leonard Susskind, Hamiltonian formulation of Wilson's lattice gauge theories, Phys. Rev. D **11**, 395 (1975).
[79] John B. Kogut, An introduction to lattice gauge theory and spin systems, Rev. Mod. Phys. **51**, 659 (1979).
[80] D. Horn, Finite matrix models with continuous local gauge invariance, Phys. Lett. B **100**, 149 (1981).
[81] Peter Orland and Daniel Rohrlich, Lattice gauge magnets: Local isospin from spin, Nucl. Phys. **B338**, 647 (1990).
[82] Indrajit Sau, Arnab Sen, and Debasish Banerjee, Weak universality induced by $Q = \pm 2e$ charges at the deconfinement transition of a $(2+1)$-dimensional U(1) lattice gauge theory, Phys. Rev. Lett. **130**, 071901 (2023).
[83] Adithi Udupa, Samudra Sur, Sourav Nandy, Arnab Sen, and Diptiman Sen, Weak universality, quantum many-body scars, and anomalous infinite-temperature autocorrelations in a one-dimensional spin model with duality, Phys. Rev. B **108**, 214430 (2023).